Reversible Navier-Stokes equation on logarithmic lattices

Guillaume Costa, Amaury Barral, and Bérengère Dubrulle*
Université Paris-Saclay, CEA, CNRS, SPEC, 91191 Gif-sur-Yvette, France

(Received 5 January 2023; revised 19 April 2023; accepted 9 June 2023; published 26 June 2023)

The three-dimensional reversible Navier-Stokes (RNS) equations are a modification of the dissipative Navier-Stokes (NS) equations, first introduced by Gallavotti [Phys. Lett. A **223**, 91 (1996)], in which the energy or the enstrophy is kept constant by adjusting the viscosity over time. Spectral direct numerical simulations of this model were performed by Shukla *et al.* [Phys. Rev. E **100**, 043104 (2019)] and Margazoglou *et al.* [Phys. Rev. E **105**, 065110 (2022)]. Here we consider a linear, forced reversible system obtained by projecting RNS equations on a log lattice rather than on a linearly spaced grid in Fourier space, as is done in regular spectral numerical simulations. We perform numerical simulations of the system at extremely large resolutions, allowing us to explore regimes of parameters that were out of reach of the direct numerical simulations of Shukla *et al.* Using the nondimensionalized forcing as a control parameter, and the square root of enstrophy as the order parameter, we confirm the existence of a second-order phase transition well described by a mean-field Landau theory. The log-lattice projection allows us to probe the impact of the resolution, highlighting an imperfect transition at small resolutions with exponents differing from the mean-field predictions. Our findings are in qualitative agreement with predictions of a 1D nonlinear diffusive model, the reversible Leith model of turbulence. We then compare the statistics of the solutions of RNS and NS, in order to shed light on an adaptation of the Gallavotti conjecture, in which there is equivalence of statistics between the reversible and irreversible models, to the case where our reversible model conserves either the enstrophy or the energy. We deduce the conditions in which the two are equivalent. Our results support the validity of the conjecture and represent an instance of nonequilibrium system where ensemble equivalence holds for mean quantities.

DOI: 10.1103/PhysRevE.107.065106

I. INTRODUCTION

In an out-of-equilibrium statistical mechanical system, achieving a steady state requires a balance between energy injection and energy dissipation. One practical example of such a system can be found in fluid mechanics, where a large-scale forcing drives a system out of equilibrium. To attain a steady state, the system must dissipate the excess energy. Such dissipation is ensured by a viscous term acting as a thermostat. This system is described by the Navier-Stokes (NS) equations, which are symmetric by time reversal in the unforced, inviscid limit. However, the presence of the viscous term breaks this time-reversal symmetry of the NS equations. When the fluid is laminar, the resulting energy dissipation is proportional to the viscosity. In the turbulent case, however, the mean dissipation becomes independent of the viscosity [1–3] suggesting a spontaneous breaking of the time-reversal symmetry. To study the validity of such an assumption, one can restore time-reversal symmetry by transforming the usual viscosity, ν, into a quantity that is odd under time reversal. There are numerous ways to do this, but the most interesting procedure is due to [4], which suggested monitoring ν so as to conserve at each time a macroscopic observable $\mathcal{G}$ (such as enstrophy [4,5] or kinetic energy [6]). Besides spontaneous symmetry breaking, this procedure allows investigation of two important questions in the context of out-of-equilibrium physics: (1) To which extent can a reversible model describe the irreversible dynamics? (2) Does the statistics of the reversible model depend on the conserved quantity? This second question refers to the possible generalization of the notion of "ensemble equivalence in equilibrium statistical mechanics," by which a system is equivalently described by microcanonical (conserved energy) or canonical (conserved temperature) ensembles. In the present case, the system is out of equilibrium due to the combination of forcing and dissipation. The equivalence between both constant energy and the constant enstrophy ensemble would then be a natural generalization of ensemble equivalence in equilibrium statistical mechanics.

These questions have been previously investigated via direct numerical simulations (DNS) of the reversible Navier-Stokes (RNS) equations. In the case of conserved energy, Shukla *et al.* [6] showed that the system undergoes a second-order phase transition, with exponents in quantitative agreement with that of a Landau mean-field theory [6]. Before the transition, the system is in a warm phase, where the system is thermalized at small scale. After the transition, the system is in a overdamped regime, where the system dynamics are dominated by viscous dissipation. At the transition, the system is in a turbulent state that bears many similarities with the stationary state of the irreversible equation, hinting at a possible positive answer to question 1 in this case. Question 2, which has never been investigated before to the best of our knowledge, will be addressed in this article.

*berengere.dubrulle@cea.fr

However, there are a number of issues that could not be addressed due to the massive numerical costs of directly simulating the NS equations. For example, it was not possible to study the importance of the resolution on the transition or the convergency of the equivalence of ensemble. In addition, some scaling properties of the dynamics at the transition could not be investigated, as the inertial range was not wide enough due to the difficulty of accommodating very small values of ν with DNS.

Motivated by these observations, we decided to extend the study of Shukla *et al.* [6] and Margazoglou [5] to a case where the RNS equations are projected on a log lattice rather than on a linearly spaced grid in Fourier space. The resulting equations correspond to a linear, forced reversible system that we call log-lattice reversible Navier-Stokes (LLRNS). We know from the work of Campolina and Mailybaev [7] that this projection allows simulations with a large resolution, at a moderate numerical cost, while the corresponding model displays most symmetries and conservation laws of the classical model on a linear grid (used for DNS with spectral methods). Moreover, the log-lattice projection makes it possible to adapt the resolution to monitor very low values of the viscosity, as already proved in [8] on the blow-up problem for the Euler equations.

The outline of the paper is as follow: we first introduce the RNS equations, followed by the projection on log lattices that we will be using to define our LLRNS model. We display our choice regarding the numerical procedure and briefly present the tools that will be useful to analyze our results, including the reversible Leith model, already used in [6]. We then go through the results and discuss the presence of a second-order transition in LLRNS and extract critical exponents. We also study the ansatz of the structure functions of LLRNS, comparing them to the case of log-lattice Navier-Stokes (LLNS) equations, where the viscosity is kept constant. We then perform a comparison between energy transfer in LLRNS and the reversible Leith model, based on a nonlinear diffusion equation in Fourier space. Finally, we study to what extent the equivalence conjectures postulated by Gallavotti [4,5] for RNS and NS equations hold in the framework of log lattices for two conservation schemes: one energy conserving and one enstrophy conserving.

II. FRAMEWORK: REVERSIBLE NAVIER-STOKES AND LOG-LATTICE PROJECTIONS

A. Reversible Navier-Stokes

The NS equations describing a fluid of viscosity ν, subject to a force $\boldsymbol{f}$, are given by

$$\partial_t \boldsymbol{u} + (\boldsymbol{u}\cdot\nabla)\boldsymbol{u} = -\nabla p + \nu\Delta\boldsymbol{u} + \boldsymbol{f}, \tag{1}$$

where $\mathbf{u}$ is the velocity, p is the pressure, and we have set the constant density equal to 1. Due to the presence of the dissipative term $\nu\Delta\boldsymbol{u}$, the dynamics induced are clearly irreversible as (1) is not left invariant under the time-reversal symmetry:

$$\mathcal{T} : t \to -t; \quad \boldsymbol{u} \to -\boldsymbol{u}; \quad p \to p. \tag{2}$$

This is true even in the presence of a force that is symmetric by time reversal (which will be the case of every forcing used in this paper).

Following the work of Shukla *et al.* [6], we introduce a reversible version of the NS equations by defining a (time-dependent) reversible viscosity ν_r, which conserves the total kinetic energy $E = \frac{1}{2}\int_{\mathcal{D}} \|\boldsymbol{u}\|_2^2 \, d\boldsymbol{x}$ over our domain $\mathcal{D}$. The expression of ν_r can be derived from an energy budget under the constraint $\partial_t E = 0$:

$$\nu_r = \frac{\int_{\mathcal{D}} \boldsymbol{f}\cdot\boldsymbol{u} \; d\boldsymbol{x}}{\int_{\mathcal{D}} \|\nabla\times\boldsymbol{u}\|_2^2 \; d\boldsymbol{x}}. \tag{3}$$

It is also possible to define another framework, where the viscosity is still time dependent, but adjusted to conserve the total enstrophy $\partial_t\Omega = 0$, where $\Omega = \int_{\mathcal{D}} \|\nabla\times\boldsymbol{u}\|_2^2 \; d\boldsymbol{x}$ [4]. The corresponding expression of the viscosity is obtained by taking the Fourier transform of (1), multiplying by $k^2\bar{\hat{u}}_i$ and summing over $\boldsymbol{k}$, leading to

$$\nu_r(\boldsymbol{u}) = \frac{\sum_{\boldsymbol{k}} \|\boldsymbol{k}\|_2^2 \hat{\boldsymbol{f}}_{\boldsymbol{k}}\cdot\hat{\boldsymbol{u}}_{-\boldsymbol{k}} + \Lambda(\hat{\boldsymbol{u}})}{\sum_{\boldsymbol{k}} \|\boldsymbol{k}\|_2^4 \|\hat{\boldsymbol{u}}_{\boldsymbol{k}}\|_2^2}, \tag{4}$$

where $\Lambda(\hat{\boldsymbol{u}})$ comes from the nonlinear term of the NS equations. While it is yet unclear whether viscid or inviscid NS equations with regular initial conditions and finite energy are subject to a finite-time blow-up, it is known that controlling the enstrophy is sufficient to prevent a blow-up [9]. Therefore, the enstrophy-conserving scheme is associated with more regular solutions than the energy-conserving scheme. In particular, it rules out a spontaneous breaking of the time-reversal symmetry mediated by dissipating singularities as conjectured by Onsager [1]. Therefore, it is interesting to explore the properties of both conservation schemes.

In the first part of this paper, we mainly focus on the conserved energy scheme, where an interesting phase transition takes place. In the second part, we analyze the Gallavotti conjecture using both conservation procedures.

Replacing the usual viscosity ν with its "reversible" counterpart ν_r in (1), we obtain the reversible Navier-Stokes (RNS) equations:

$$\partial_t \boldsymbol{u} + (\boldsymbol{u}\cdot\nabla)\boldsymbol{u} = -\nabla p + \nu_r\Delta\boldsymbol{u} + \boldsymbol{f}. \tag{5}$$

Taking into account that $\boldsymbol{f}$ is invariant by the time-reversal symmetry, it is then easy to check that the whole equation is also invariant by the symmetry (2), hence its name.

Since the viscosity is no longer a constant, the Reynolds number $\mathrm{Re} = \frac{LU}{\nu}$ is no longer as a valid control parameter. Therefore, in the fixed energy case we introduce the dimensionless control parameter $\mathcal{R}_r$ [6] given by

$$\mathcal{R}_r = \frac{f_0}{E_0 k_f}, \tag{6}$$

where f_0 is the forcing amplitude, $k_f = \frac{2\pi}{L_f}$ the wave number at which the forcing occurs, and E_0 the constant, total kinetic energy.

B. LLRNS model on log lattices

Our LLRNS model is obtained by projecting the reversible equations (5) onto a discretized logarithmic grid, composed of exponentially spaced modes (Fig. 1):

$$k = k_0\lambda^n,$$

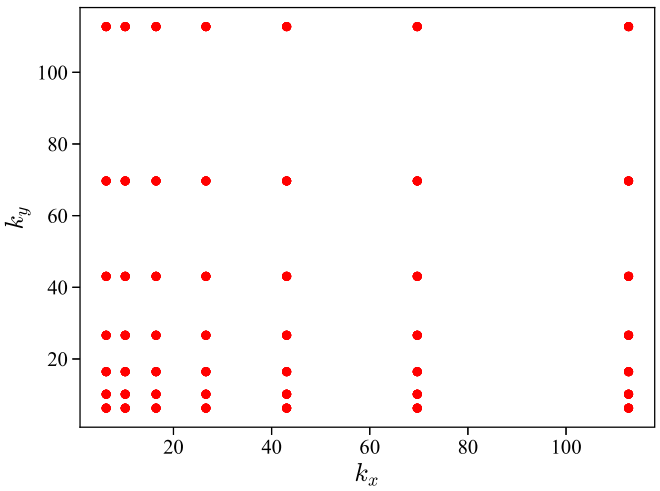

FIG. 1. Geometry of the logarithmic lattices. Example of modes on a 2D log lattice with a spacing parameter $\lambda = \phi \approx 1.618$.

where λ is the log-lattice spacing parameter. This construction is detailed by Campolina and Mailybaev [7,8]. We start by taking the Fourier transform of Eq. (5), to get the RNS equations in spectral space:

$$\partial_t \hat{u}_i + \boldsymbol{i} k_j \hat{u}_j * \hat{u}_i = -\boldsymbol{i} k_i \hat{p} - \nu_r k_j k_j \hat{u}_i + \hat{f}_i, \tag{7}$$

where Einstein summation over repeated indices is used, $\boldsymbol{i}$ is the square root of -1, k_i is the ith component of the wave number $\mathbf{k} = (m, n, q)\mathbf{k}_0$, $\hat{g}$ is the Fourier transform of g, and $*$ is the convolution product which couples modes in triadic interactions such that $\boldsymbol{k} = \boldsymbol{p} + \boldsymbol{q}$.

We then project this equation onto the log lattice. For this, we consider from now on that the velocity modes $\hat{u}_i$ depend on only the wave vectors on the log lattice. This projection is then valid provided that the convolution operator is "well-defined," i.e., that it respects the symmetries of a convolution operator and has a nonempty set of triadic interactions. We thus require that

$$\lambda^m = \lambda^n + \lambda^q, (\mathrm{m,n,q}) \in \mathbb{Z}^3 \tag{8}$$

admits solutions, which restricts the values of λ to three families of solutions, each having z interactions in D dimensions:

(i) $\lambda = 2$ ($z = 3^D$)

(ii) $\lambda = \sigma \approx 1.325$, the plastic number ($z = 12^D$)

(iii) λ such that $1 = \lambda^b - \lambda^a$ for some integers $0 < a < b$. $(a, b) \neq (1, 3), (4, 5)$ with $\gcd(a, b) = 1$ ($z = 6^D$).

Note that for the lowest possible values of a and b, which is (1,2), λ is the golden number ($\phi \approx 1.618$). The 2D geometry of such a lattice is shown in Fig. 1.

Besides the convolution product, log lattices are also endowed with a scalar product given by

$$(f, g) = \mathrm{Re}\left(\sum_{\boldsymbol{k}} f(\boldsymbol{k})\overline{g(\boldsymbol{k})}\right). \tag{9}$$

Our LLRNS model is then defined by the set of ODE's (7), with viscosity being given by Eq. (3) or (4), and by the choice of λ among the possible values that follow from Eq. (8). Each configuration corresponds to a reversible nonlinear out-of-equilibrium model whose conservation laws and symmetries are very close to that of the RNS equations.

C. Quantities of interest

1. Generic quantities

In the fixed energy case, the enstrophy Ω and the reversible viscosity ν_r are good candidates for the order parameter, while $\mathcal{R}_r$ (6) is a good control parameter.

Throughout our study, we can compute two large-scale quantities of interest:

(i) The energy spectrum $E(k, t) = \frac{1}{(\lambda-1)kN_k} \sum_{k \leqslant |\boldsymbol{k}'| < \lambda k} \times \|\hat{\boldsymbol{u}}(\boldsymbol{k}', t)\|_2^2$, where N_k is the number of points in the shell of radius k [proportional to $\log^2(k)$].

(ii) The total enstrophy $\Omega(t) = \sum_k k^2 E(k, t)$.

We also compute the mean energy transfer at scale k through

$$\Pi(k) = \langle -2\Im(\boldsymbol{u}, \boldsymbol{k} \cdot \boldsymbol{u} * \boldsymbol{u})\rangle, \tag{10}$$

and an ansatz of the structure functions, using the following convention:

$$F_q(k) = \left\langle \left\|\hat{\boldsymbol{u}}(\boldsymbol{k}, t)\right\|_2^q \right\rangle, \tag{11}$$

where $\|\mathbf{k}\|_2 = k$ and $\langle\cdot\rangle$ refers to temporal averages over shells of radius k.

2. Leith model

The Leith model is a toy model based on a nonlinear diffusive equation, which in its inviscid description [10] approximates the dynamics of the energy spectrum of a Euler flow. It exhibits both an inertial domain with scaling $k^{-5/3}$ and a quasithermalization at small scales characterized by a Gibbsian equipartition with scaling $E(k, t) \propto k^2$. Such a model is described by a well-chosen second-order diffusive operator:

$$\partial_t E(k, t) = -\partial_k \Pi(k, t) - \nu k^2 E(k, t),$$
$$\Pi(k, t) = -Ck^{11/2}\sqrt{E(k, t)}\partial_k\left(\frac{E(k, t)}{k^2}\right).$$

Note that C is a dimensional constant that we set to 1 in this article.

This model has been adapted by [6] to accommodate reversible viscosities by changing ν into ν_r, given by Eq. (3). Its solutions confirm the existence of a mean-field second-order phase transition, albeit for an order parameter equal to $\sqrt{\Omega}$. Moreover, it showed that the resolution of the simulation could have a large impact on the nature of the transition, the latter becoming imperfect as the resolution is decreased. In this article we adopt the same convention for the dimensionless number representing the influence of resolution, namely, $h = k_0/k_{\max}$, where k_0 and $k_{\max}$ are, respectively, the minimum and maximum wave number in our simulation.

In our system the thermalization is no longer associated with an energy spectrum following $E(k, t) \propto k^2$ but instead to a k^{-1} behavior. It is then necessary to adapt the previous definition of the energy transfer to our system:

$$\Pi(k, t) = -Ck^{5/2}\sqrt{E(k, t)}\partial_k[kE(k, t)].$$

Solving $\partial_k \Pi(k,t) = 0$, we obtain an energy spectrum of the form $E(k,t) \propto (Ak^{-5/2} + Bk^{-3/2})^{2/3}$, where (A, B) are two constants taking into account boundary conditions and governing the scale at which the thermalization occurs.

D. Numerical framework

1. Integration scheme

We integrate (7) using a three-step method. Starting from the initial conditions $\hat{u}(t)$, we first solve the equation without any viscosity using an explicit adaptive Runge-Kutta method of order 4–5 via the DOPRI5 solver from the Python library Scipy. The equation solved is

$$\partial_t \hat{u}_i = P_{ij}(-ik_q \hat{u}_q * \hat{u}_j + \hat{f}_j), \tag{12}$$

where $P_{ij} = \delta_{ij} - \frac{k_i k_j}{k^2}$ accounts for the pressure term under zero divergence hypothesis. This gives us $\hat{u}(t+dt)_{\nu_r=0}$ where dt is the time step. To maintain a very high degree of accuracy for our conservation laws, we do not use the expression for reversible viscosity given by Eq. (3) or (4), but instead compute in a second step the reversible viscosity ν_r by numerically solving $\mathcal{G}(\nu_r, t+dt) = \mathcal{G}_0$, where $\mathcal{G}$ stands for the conserved quantity. The final step is to apply the chosen viscosity by a technique similar to viscous splitting: $\hat{u}(t+dt) = \hat{u}(t+dt)_{\nu_r=0} e^{-\nu_r k^2 dt}$.

We provide in Appendix A a comparison between this method and direct computation using the analytical expression of ν_r (3) in the Runge-Kutta solver.

2. Numerical details

The minimum wave number of the grid is set to $k_{\min} = 2\pi$. The maximum grid size $N = 20^3$ is chosen such the hydrodynamic branch is well enough resolved. We set a maximum time step $dt = 0.005$, in order to avoid underresolving some very stiff moments when the viscosity tends to zero. As a result, whenever the viscosity is not very small, the time step is a constant equal to dt.

The equation $\mathcal{G}(\nu_r, t+dt) = \mathcal{G}_0$ is solved such that $\mathcal{G}$ is conserved with floating-point accuracy: $|\mathcal{G}(t+dt) - \mathcal{G}_0| < 10^{-14}\mathcal{G}_0$.

We use the following initial conditions, taken from [6]:

$$\begin{aligned} \hat{u}_x(\mathbf{k}) &= U(\boldsymbol{k}), \\ \hat{u}_y(\mathbf{k}) &= -\hat{u}_x(\boldsymbol{k})\frac{k_x}{k_y}, \\ \hat{u}_z(\mathbf{k}) &= 0, \end{aligned} \tag{13}$$

where U is an initial field, with initial energy centered on the large scales.

The forcing term $\boldsymbol{f}$ is a constant field of norm f_0, symmetric by time reversal, with nonzero contributions for $\boldsymbol{k}$ such that $15 < \|\boldsymbol{k}\|_2 < 16$:

$$\begin{aligned} \hat{f}_x(\mathbf{k}) &= f_0 \text{ if } 15 < \|\boldsymbol{k}\|_2 < 16 \text{ else } 0, \\ \hat{f}_y(\mathbf{k}) &= f_0 \text{ if } 15 < \|\boldsymbol{k}\|_2 < 16 \text{ else } 0, \\ \hat{f}_z(\mathbf{k}) &= 0. \end{aligned} \tag{14}$$

Unless written otherwise, the log-lattice spacing parameter is $\lambda = \phi$. The range of parameters studied is chosen such that it is possible to observe the two regimes previously observed by Shukla *et al.*

All the simulations ran on one core of a consumer-grade computer, for a few (<4) CPU days at most.

III. RESULTS

All the results presented in this paper before Sec. III G are obtained in the conserved energy case, i.e., for $\mathcal{G} = E$.

A. Dynamics

Figure 2(a) illustrates the time evolution of the normalized enstrophy $\tilde{\Omega}$ (properly defined in Appendix B) for many modes $N = 20^3$. As in [6], different regimes are observed. At low values of the control parameter $\mathcal{R}_r$, the solutions converges to a constant mean value of $\tilde{\Omega}$ with few to no fluctuations. This regime is associated with a lower branch of mean viscosity $\langle \nu_r \rangle$ [Fig. 2(b)] that develops a power law $\langle \nu_r \rangle \propto \mathcal{R}_r^{\alpha}$, where $\alpha \approx 2$. This result was already obtained in DNS [6] and can be justified using a Kubo fluctuation dissipation theorem, which also applies on log lattices. As the size of the grid increases, it becomes harder to reach the limit $\mathcal{R}_r \to 0$ as the low values of viscosity require smaller time steps. This limit is associated with a thermalized steady state, as it is characterized by a vanishing energy injection and therefore, in order to conserve the energy, to a vanishing viscosity.

As $\mathcal{R}_r$ increases, the system fluctuations continually increase up to a certain value of $\mathcal{R}_r^*$ at which fluctuations reach their maximum. Beyond this critical value, fluctuations slowly decrease to zero, towards a lower branch of enstrophy [Fig. 2(a)]. This branch corresponds to a branch of large viscosity [Fig. 2(b)]. Before vanishing completely, the enstrophy fluctuations appear as "bursts" of enstrophy.

Note that defined in such a way, $\mathcal{R}_r^*$ depends on the resolution N. Indeed, both the value of $\mathcal{R}_r$ at which the system leaves the collapsed branch]Fig. 2(b)] and the location of maximum fluctuations [Fig. 3(d)] clearly depend on the resolution. Also note that both definitions of $\mathcal{R}_r^*$ [from fluctuations and the asymptote in Fig. 2(b)] are equivalent in the limit $N \to \infty$ as the thermalized branch can never be reached.

B. Phase transitions

In Shukla *et al.* [6] the various regimes of the enstrophy dynamics are associated with the existence of a second-order phase transition, described by a Landau mean-field theory. Specifically, the time-averaged normalized enstrophy $\langle \tilde{\Omega} \rangle$ exhibits a power law $\langle \tilde{\Omega} \rangle = (1 - \frac{\mathcal{R}_r}{\mathcal{R}_r^*})^{\beta}$, with $\beta \simeq 0.5$, while the normalized standard deviation of the renormalized enstrophy $\sigma_{\tilde{\Omega}}$ presents a divergence around $\mathcal{R}_r^*$, following a power law $\sigma_{\tilde{\Omega}} = (1 - \frac{\mathcal{R}_r}{\mathcal{R}_r^*})^{-\gamma}$ with $\gamma \simeq 1$. As it is possible to observe different values of γ on each side of the transition, we define γ_l and γ_r where l and r stand for left and right, respectively.

In our case we also observe at $N = 20^3$ behaviors for the enstrophy that are reminiscent of a second-order phase transition, albeit with exponents that do not correspond to the mean-field description [Figs. 3(a) and 3(c) and Table I]. Indeed, we observe a power law with exponent $\beta \simeq 1$, which

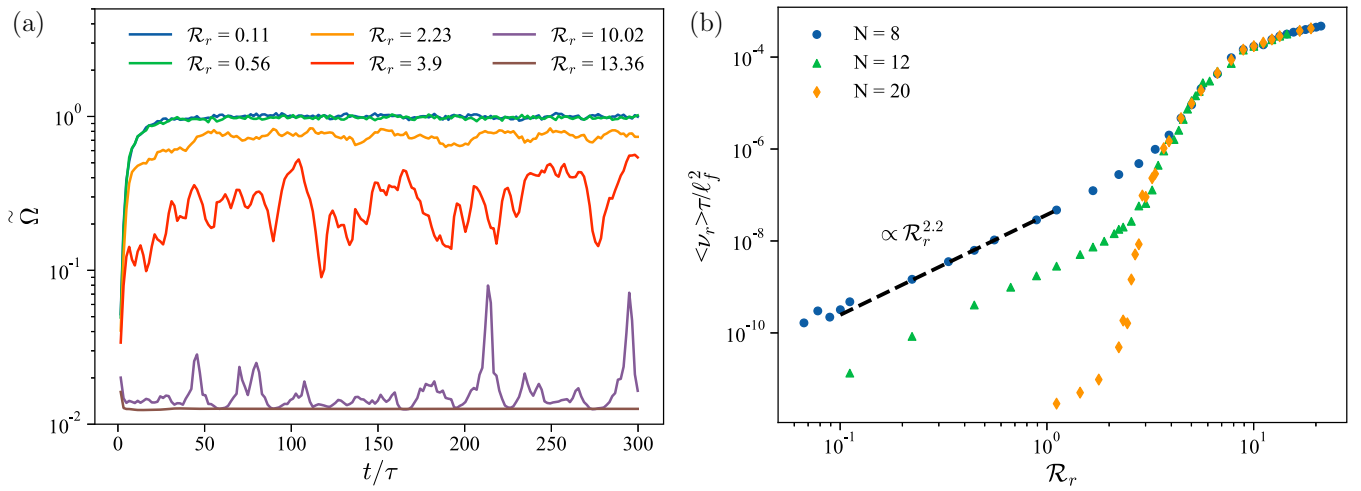

FIG. 2. Behaviors of order parameters using $\lambda = \phi$. (a) Time series of the normalized enstrophy $\widetilde{\Omega}$ for different values of the control parameter $\mathcal{R}_r$, with $N = 8^3$. (b) Time-averaged reversible viscosity as a function of the control parameter $\mathcal{R}_r$. The dashed line represents a linear fitting in the warm regime, exhibiting a power-law behavior. The dimensionless time is $\tau = \ell_f/\sqrt{E_0}$, where ℓ_f is the scale at which the forcing occurs.

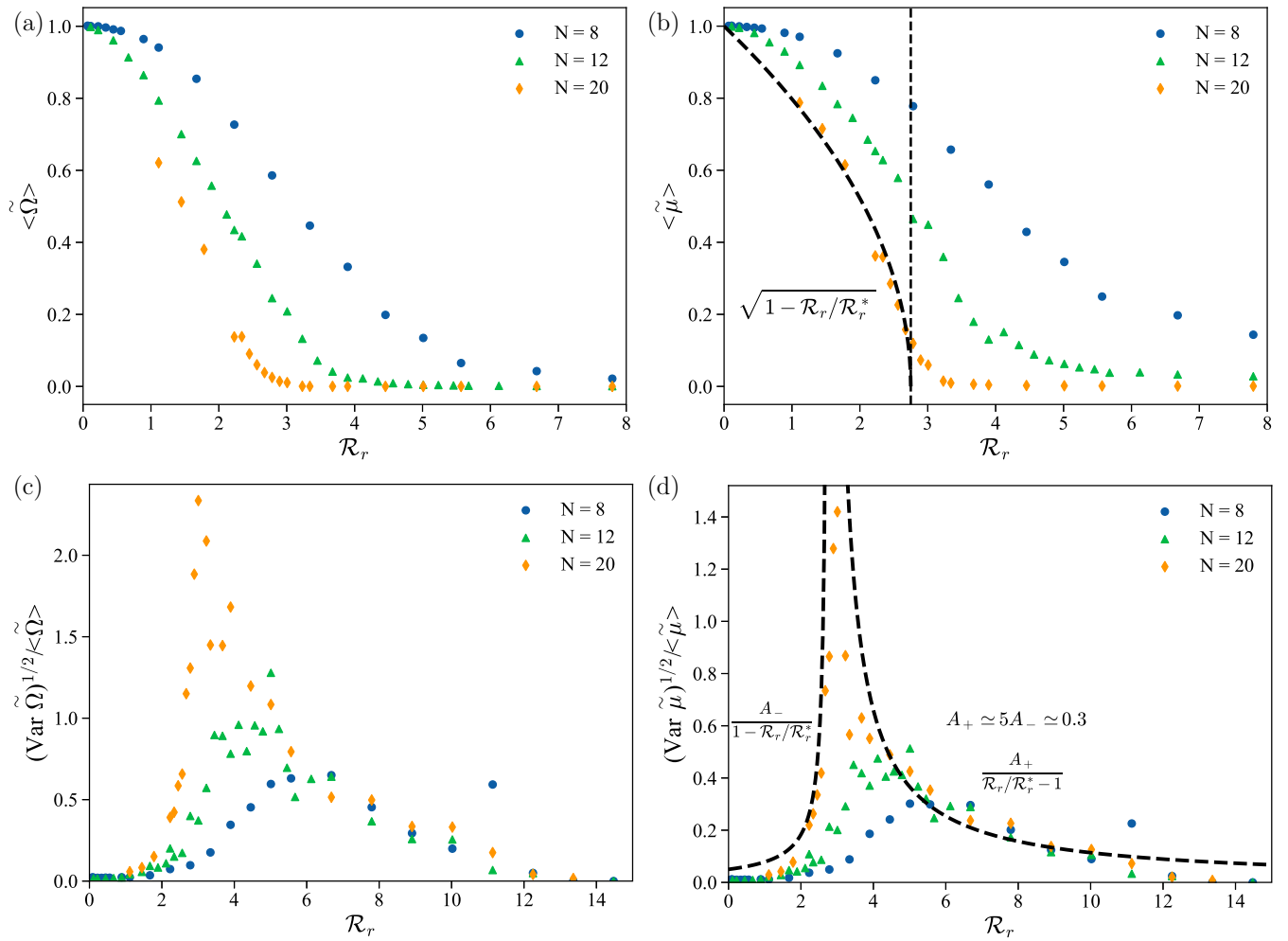

FIG. 3. Second-order transition for $\lambda = \phi$. Evolution of (a) the renormalized mean enstrophy and (b) $\tilde{\mu}$ as a function of $\mathcal{R}_r$. Variance of (c) the renormalized enstrophy and of (d) $\tilde{\mu}$ as a function of $\mathcal{R}_r$. The dashed lines associated with the equations correspond to a Landau mean-field formulation of the phase transition.

TABLE I. Critical exponents of $\widetilde{\Omega}$ as a function of h. For $\lambda = 2$, values of γ_r were not extracted as the variance does not vanish, but converges to a constant on a domain extending quite far away from $\mathcal{R}_r^*$.

λ	N	h	β	γ_r	γ_I
	8^3	7×10^{-3}	–	–	–
2	12^3	4×10^{-4}	$\simeq0.8$	–	1.6
	16^3	3×10^{-5}	$\simeq1$	–	1.0
	8^3	3×10^{-2}	–	1.0	2.2
ϕ	12^3	5×10^{-3}	$\simeq0.5$	1.0	1.8
	20^3	1×10^{-4}	$\simeq1$	1.0	1.0
Shukla *et al.* [6]	128^3	2.4×10^{-2}	$\simeq0.5$	$\simeq1$	$\simeq1$
Landau mean field	–	–	0.5	1	1

TABLE II. Critical exponents of $\tilde{\mu}$ as a function of h. Values of γ_r were not extracted as the variance does not vanish, but converges to a constant on a domain extending quite far away from $\mathcal{R}_r^*$.

λ	N	h	β	γ_r	γ_I
	8^3	7×10^{-3}	–	–	–
2	12^3	4×10^{-4}	$\simeq0.4$	–	1.6
	16^3	3×10^{-5}	$\simeq0.5$	–	1.0
	8^3	3×10^{-2}	–	1.0	1.6
ϕ	12^3	5×10^{-3}	$\simeq0.27$	1.0	1.4
	20^3	10^{-4}	$\simeq0.5$	1.0	1.0

is larger than its mean-field version [Fig. 3(a)]. In the case of the variance, we observe a divergence at $\mathcal{R}_r^*$ with a critical exponent corresponding to the mean-field value $\gamma_I = 1$, like in [6].

Our results show that, while the nature of the transition is unaffected by the details of the interactions between modes, the value of the critical exponents depends on those details. One should see Table I for different values of λ and recall that on log lattices, different values of λ correspond to different numbers of local interactions.

In that respect, it is interesting to see whether our result fits in the cruder description of the interactions provided by the Leith model. In this model the mean-field description is found by taking the square root of the enstrophy as an order parameter. In our case, upon defining $\tilde{\mu} = \widetilde{\Omega}^{1/2}$, we indeed observe a mean-field behavior for $\langle\tilde{\mu}\rangle$ in the limit of large grids $k_{\max} \to \infty$ [e.g., Figs. 3(b) and 3(d)]. Its critical order parameters depend on the lattice spacing λ as $\mathcal{R}_r^* \approx 3.75$ for $\lambda = 2$ and $\mathcal{R}_r^* \approx 2.75$ for $\lambda = \phi$. The computed exponents associated with this model are presented in Table II. Note, however, that the mean-field description is not entirely valid in our model, as we do not observe the peculiar link between pre- and posttransitions prefactors: $A_+ = 2A_-$. Still, it seems that as the number of interactions grows (i.e., as λ decreases), we are getting closer and closer to this description.

Finally, we stress that as soon as $\mathcal{R}_r > \mathcal{R}_r^*$, both the variance and the mean viscosity [Fig. 2(b)] become independent of the grid size. Therefore, only β and γ_I depend on $k_{\max}$.

C. Characterizing the various phases with spectra

As shown in [6], the nature of the different phases before and after the transition can be elucidated by looking at energy spectra. Examples are provided in Fig. 4. Before the transition, we observe a spectrum that is characterized by two slopes: one at low wave numbers, with an exponent close to $-5/3$, and one at large wave numbers, with an exponent closer to -1. As already discussed in [7,11], the -1 slope corresponds to thermalization on log lattices, characterized by equipartition of energy among the modes. The $-5/3$ regime corresponds

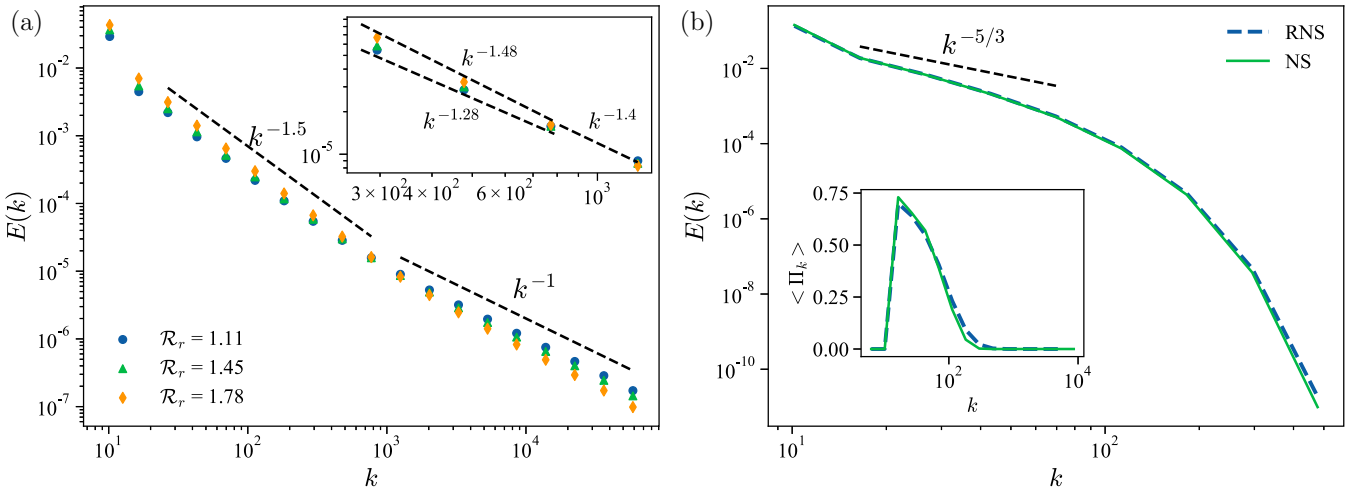

FIG. 4. Time-averaged energy spectra vs $\mathcal{R}_r$, $\lambda = \phi$, $N = 20^3$ modes. (a) Warm regime, with coexistence of two phases. The dotted line represents the slope of the two coexisting regimes, a pseudo-Kolmogorov regime at large scales and a thermalized regime at small scales exhibiting a -1 slope. The inset shows a zoom in the crossover area, highlighting the difference in slopes with respect to $\mathcal{R}_r$ associated to the contamination of the bigger scales by the thermalization. (b) Laminar state, with dominant dissipative range, and no thermalization. The inset shows the energy transfer Π_k.

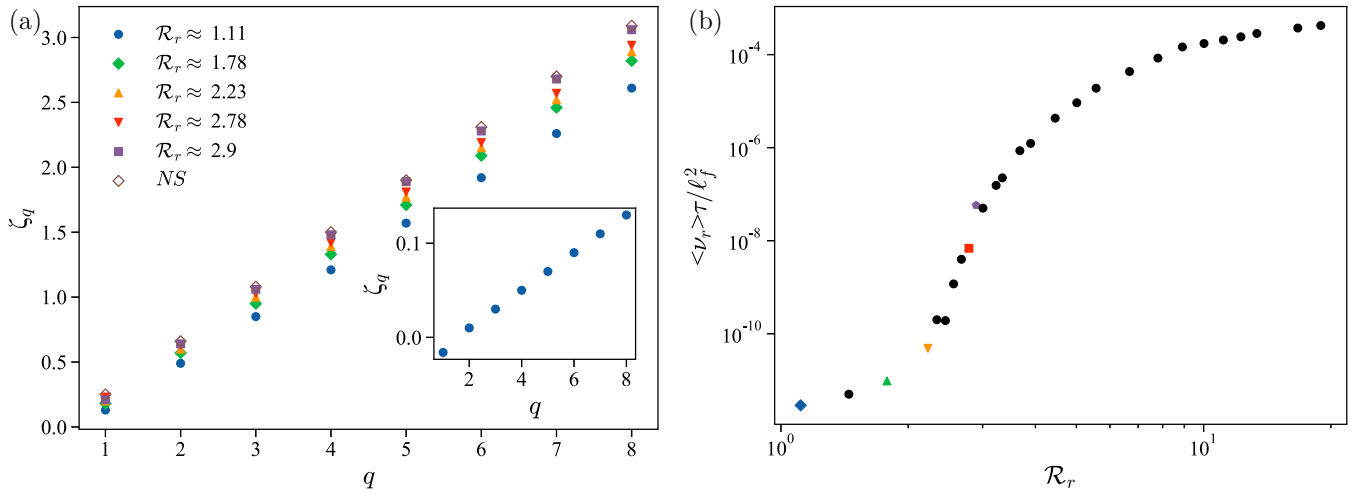

FIG. 5. Extracted exponents of the structure functions and localization in the transition for $\lambda = \phi$, $N = 20^3$ modes. Both figures share the same legend. (a) Exponents of the structure function of order q for various RNS simulations and comparison to a NS simulation. The inset presents the exponents, extracted at small scales, in the case of a quasithermalized state. (b) Color-coded version of the ν_r vs $\mathcal{R}_r$ diagram, showing where the various results are located with respect to the transition. The colors of the data points are the same as those from panel (a).

to a classical spectrum due to a positive flux of energy, as evidenced by the insert of Fig. 4(b). We call this phase with a coexistence of two cascades the "warm cascade" regime. As $\mathcal{R}_r$ decreases, the thermalized phase extends further towards lower k, and the pseudo-Kolmogorov phase disappears. Conversely, as $\mathcal{R}_r$ increases, the thermalized phase progressively disappears, to leave room for an increasingly laminar state as the reversible viscosity increases. Such a state is shown in Fig. 4(b).

D. Structure functions

The nature of the various phases can be further characterized using higher orders of the velocity field, via the structure functions [Eq. (11)]. In classical shell models, such structure functions are subject to intermittency, as they exhibit scaling laws $F_q(k) \sim k^{-\xi_q}$ that deviate from the monofractal behavior $\xi_q = q\xi_1$ [12–15].

In our case it is difficult to measure the exponents of the structure functions for all phases: at large values of $\mathcal{R}_r$ the viscosity rises quickly, and the inertial range becomes very small. At small values of $\mathcal{R}_r$, the scaling laws are polluted by the coexistence of the pseudo-Kolmogorov regime and the thermalized state, as illustrated in Fig. 4(a). This invalidates the classical method of computing exponents via extended self-similarity [16] as the structure functions can present multiple slopes at different scales. We extracted exponents via the following method: we first determine the inertial range by computing the time-averaged energy transfer Π_k through Eq. (10). Then we define the inertial range as the range of wave numbers where it is flat. If this range is large enough (at least a decade), we fit the scaling exponents of the structure functions on this range only. This provides us with an unambiguous determination of ξ_q. The extracted exponents are shown in Fig. 5(a), for the value of $\mathcal{R}_r$ in various regimes, as illustrated in Fig. 5(b).

In the limit of low $\mathcal{R}_r$, the ξ_q exponents appear to be significantly lower than the usual exponents (Fig. 5, blue, green, and orange curves). This phenomenon can be explained by the fact that, in such a limit, the system tends to follow equipartition, associated with an energy spectrum of $E(k) \sim k^{-1}$ (Fig. 4). This is indeed what we observe: as $\mathcal{R}_r$ gets closer to 0 a quasithermalized spectra appears, first at low scales, and then progresses towards the larger scales, impacting the slope even at larger scales [as illustrated in Fig. 4(a) and the inset of Fig. 5(a)]. There is no intermittency in this regime, with all exponents aligning onto a perfect line. In the other limit, as $\mathcal{R}_r$ rises, the RNS exponents increase (Fig. 5). However, there is still no intermittency in this regime. To check whether it was a feature of the RNS system, we computed the same exponents from a simulation of NS equations with fixed viscosity. The result is also shown in Fig. 5(a) (brown curve). We see that the resulting exponents are very close to the exponents we observe in RNS, reaching a quasiperfect agreement for both exponents and slope (Table III) located around the middle of the transition area.

This absence of intermittency is not surprising, as log-lattice models consider only local interactions. Such a phenomenon was also observed in REWA models of turbulence, where intermittency decreases as the number of interactions decreases [17–19]. In contrast, intermittency has already been observed in various shell models such as SABRA [20] or GOY [21] models. In that case, it was observed that the tuning of the free parameter controlling

TABLE III. Slopes of the exponents of the structure functions for both RNS and NS equations. Values were extracted by fitting the structure functions in the inertial range, determined by the domain of constant energy transfer.

Equation	RNS					NS
$\mathcal{R}_r$	1.11	1.78	2.23	2.78	2.9	–
Slope	0.36	0.38	0.4	0.4	0.42	0.42

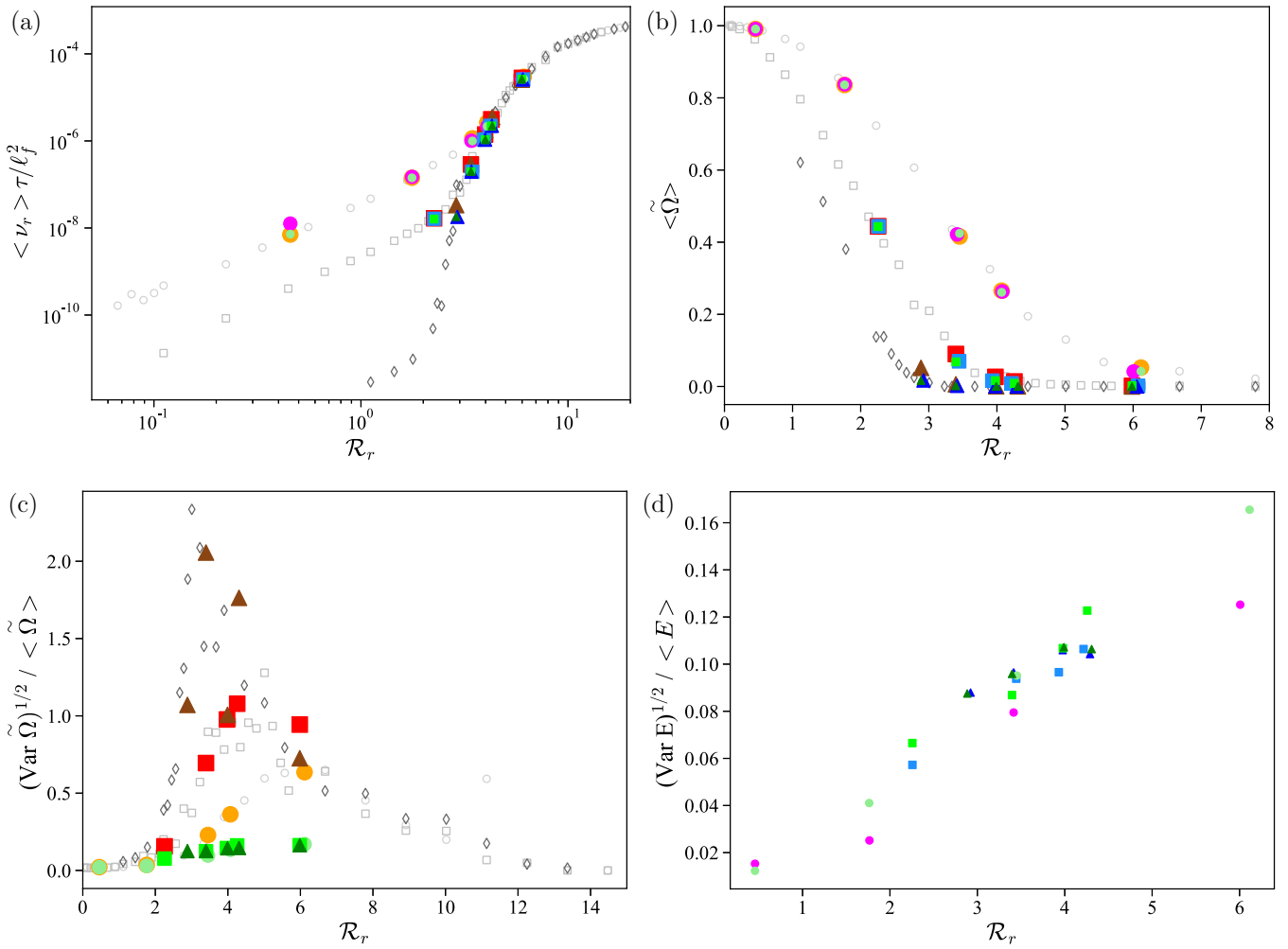

FIG. 6. Existence of a phase transition in the different systems for different order parameter. (a) Renormalized viscosity function of the previously introduced control parameter $\mathcal{R}_r$. (b) Renormalized enstrophy as a function of the control parameter $\mathcal{R}_r$. (c) Rescaled variance of the normalized enstrophy as a function of $\mathcal{R}_r$. (d) Rescaled variance of the energy, as a function of $\mathcal{R}_r$, for the LLRNS conserved enstrophy case and LLNS. In all four figures, the empty gray symbols are the data of Figs. 2(b) and 3(a). Circles, squares, and triangles are associated to $N = 8^3$, 12^3, and 16^3, respectively. The conservation schemes are coded by color, with light green to dark green being the irreversible LL-Navier-Stokes model, purple to dark blue the LLRNS model with conserved enstrophy, and orange to brown the LLRNS model with conserved energy. Note that in the nonconserved energy case, we define $\mathcal{R}_r$ using the averaged kinetic energy. Also note that the difference between the gray and blue symbols lies in the numerical details; both are associated with the conserved energy case. Gray symbols are obtained varying the forcing amplitude f_0, while blue symbols are associated with a fixed f_0 and varying initial condition, i.e., varying E_0. Panels (a) and (b) show that all mean viscosities and enstrophy collapse on an universal law, while Fig(c) and (d) highlight the absence of transition for LL-Navier-Stokes and LL-RNS with conserved enstrophy.

additional conservation can bring the system from a situation where the only fixed point is the K41 scaling (no intermittency) to a situation where the K41 scaling becomes unstable, leading to chaos and intermittency [21]. In our case, it is likely that with $\lambda = \phi$ we are in the first situation, with only one stable fixed point. It would be interesting to check whether decreasing the value of λ results in the loss of stability of the fixed point and the appearance of intermittency. This is beyond the scope of this article, however, and left for future work.

Note finally that in the log-lattice simulations, the usual Kolmogorov prediction $\xi_q \propto q/3$ does not hold. Indeed, even for the NS equations, the slope is roughly equal to 0.42 (Table III).

E. Universal and nonuniversal laws

In previous sections, we described the dependence of $\langle\nu\rangle\tau/\ell_f^2$ (or $\langle\tilde{\Omega}\rangle$) on $\mathcal{R}_r$ for LLRNS models with constant energy. Surprisingly, such behavior extends to both LLRNS models with conserved enstrophy and to irreversible LL-Navier-Stokes models (Fig. 6) upon defining $\mathcal{R}_r = \frac{f_0}{\langle E\rangle k_f}$. This property is interesting as it provides information on the steady state of the system, and on whether the system is well resolved. Indeed, if the system is underresolved (i.e., $k_{\max} \ll k_\eta$, k_η being the Kolmogorov scale), it is characterized by a thermalization of the small scales and corresponds to a state located before the transition at $\mathcal{R}_r < \mathcal{R}_r^*$, on the linear part of Fig. 6(a).

However, neither the LLRNS with conserved enstrophy nor the LL-Navier-Stokes model displays the divergence of fluctuations observed in the LLRNS with fixed energy [see Fig. 3(d)]. Indeed, the LL-Navier-Stokes model exhibits bounded values of energy and enstrophy fluctuations, as shown in Figs. 6(c) and 6(d). The LLRNS model with constant enstrophy cannot, by construction, display any enstrophy fluctuations. However, it does not present diverging fluctuations for the energy either [see Fig. 6(d)]. This shows that the phase transition feature observed in the LLRNS model with constant energy is nontrivial. We conjecture that these events are linked with the existence of events of quasi-blow-up in the vorticity, which are naturally present in the inviscid blow-up [22,23]. These quasi-blow-ups can propagate from low wave numbers to large wave numbers when the viscosity is low, provoking events of large vorticity. In the case where the enstrophy is fixed, such quasi-blow-ups cannot exist anymore. In addition, these events are blocked by normal constant viscosity, but not by hypoviscosity [23]. A time-dependent viscosity like in the RNS case could be viewed as a hypoviscosity, leaving room for these events to develop, in contrast with LL-Navier-Stokes. This therefore explains why we only observe these events in the LLRNS with constant energy.

F. Comparison with Leith model predictions

1. Influence of the resolution

While performing simulations on log lattices, it is possible to reach high resolutions ($k > 10^{20}$) at a moderate numerical cost, making it possible to analyze the effect of the resolution on the transition. Such a study could not be done using DNS.

A first influence of resolution can be obtained on the value of the mean reversible viscosity, illustrated in Fig. 2(b): as $k_{\max}$ (or equivalently the number of modes, N) is increased, the viscosity decreases for a same value of $\mathcal{R}_r$, as there is more room for the cascade to operate. Therefore, the time-averaged viscosity gives us some insights on the dependence of the system on the resolution. Indeed, before the transition, for $\mathcal{R}_r < \mathcal{R}^*_{r,-}$ (being the lower bound of the transition) the viscosity exhibits a very large dependence on the size of the grid. As we reach the transition area, which we locate at the beginning of the quick rise of viscosity, all the data then collapse on the same universal curve, independent of $k_{\max}$. Note that $\mathcal{R}^*_{r,-}$ shifts to lower values as the size of the grid increases (Table IV).

Another influence of the resolution is given by the nature of the transition, which shifts from a second-order transition to an imperfect transition as the number of modes is decreased [see Figs. 3(c) and 3(d)]. This effect was a prediction of the Leith model introduced in [6], and we observe the same typical features found in this model.

Indeed, for $N < 20^3$, neither the mean enstrophy nor its square root follows a power law. Such description is accurate only upon reaching $N = 20^3$. In the case of the variance, we observe in Fig. 3(d) a scenario that resembles the one predicted by the Leith model: at low resolution, the standard deviation exhibits a "bump" [Fig. 3(d), circle and triangle markers]. In this case, extracting a γ exponent is questionable. Nevertheless, Table I gathers all the extracted critical exponents. At larger resolution, the divergence of the variance becomes more visible, with a critical exponent converging to the mean-field value $\gamma_l = 1$. Note that even while using log lattices, there are still finite-size effects, as the limit $\mathcal{R}_r \to 0$ exhibits truncated Euler dynamics, characterized by equipartition $E(k) \propto k^{-1}$ (Fig. 4).

TABLE IV. Values of various quantities around the transition area. $\mathcal{R}^*_{r_-}$ defines the value at which the transition area starts, defined by the quick rise in viscosity. $\Delta\nu$ represents the difference in viscosity between the two asymptotic regimes separated by the transition area. $h = \frac{k_0}{k_{\max}}$ is a parameter used to quantify the influence of the resolution, and N is the number of spectral modes.

λ	N	h	$\Delta\nu_r$	$\mathcal{R}^*_{r_-}$	$\mathcal{R}^*_r$
	8^3	7×10^{-3}	10^4	$\approx$4.3	$\approx$7
2	12^3	4×10^{-4}	10^6	$\approx$3.6	$\approx$5
	16^3	3×10^{-5}	10^8	$\approx$3.1	$\approx$3.75
	8^3	3×10^{-2}	10^2	$\approx$4.4	$\approx$5
ϕ	12^3	5×10^{-3}	10^4	$\approx$2.8	$\approx$4
	20^3	10^{-4}	10^8	$\approx$1.8	$\approx$2.75
Shukla *et al.* [6]	128^3	2.4×10^{-2}	–	$\simeq$2.0	2.75

2. Further comparison with the Leith model

It appears that, so far, our results and observations are in general agreement with the reversible Leith model proposed in [6]. It is then interesting to compare more quantitatively those two systems. The only quantity from the RNS runs that can be compared to the Leith model is the energy transfer. Therefore, our comparison will rely on computing the Leith-like energy transfers Π_{Leith} (see Sec. II C 2) from the RNS energy spectra and comparing them to the RNS transfers Π_{RNS}.

The comparison between the two quantities is presented in Fig. 7. We see that the Leith-like transfer is able to mimic the RNS transfer in the inertial domain, but drops more quickly in the dissipative domain. This effect is probably caused by the Leith-like computation not taking into account the strong oscillations of the viscosity (and therefore of the Kolmogorov length) naturally present in RNS. Such oscillations tend to straighten the transfer a bit further outside the inertial range. Overall, it seems that the Leith models share features with the RNS equations without completely reproducing their dynamics.

G. Gallavotti conjecture

In this section we now investigate how relevant the reversible models are to understand the dynamics of the irreversible LL-Navier-Stokes model. This can be done via suitable adaptation of conjectures by Gallavotti [5].

1. Definitions and conjectures

Following [5], we introduce the collection $\mathcal{E}^{\mathcal{I},N}$ of the stationary distributions $\mu_\nu^{\mathcal{I},N}$, where $\mathcal{I}$ characterizes the irreversible equation (with time-independent viscosity, i.e., LL-Navier-Stokes), with N modes. Similarly, we define the collection $\mathcal{E}^{\mathcal{R},N}$ of the stationary distributions $\mu_G^{\mathcal{R},N}$, associated with the LLRNS model of N modes, where G is the conserved quantity (total enstrophy, total kinetic energy, etc.).

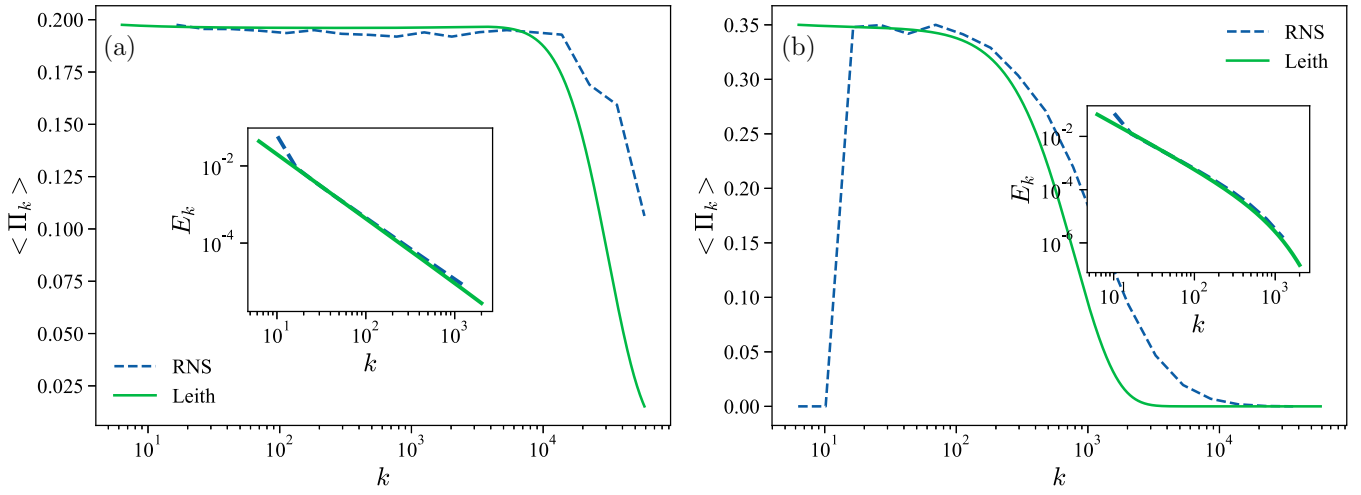

FIG. 7. Quantitative comparison of the energy transfers between RNS (dashed lines) and Leith-like transfers (full lines). The main figures present the two energy transfers, while the insets show the fitted energy spectra. The two figures are obtained for different values of $\mathcal{R}_r$ (a) $\mathcal{R}_r \approx 2.23$ (b) $\mathcal{R}_r \approx 3.34$.

For any observable $\mathcal{O}$, $\langle \mathcal{O} \rangle_\nu^{\mathcal{I},N}$ and $\langle \mathcal{O} \rangle_\mathcal{G}^{\mathcal{R},N}$ denote the averages over the distributions $\mu_\nu^{\mathcal{I},N}$ and $\mu_G^{\mathcal{R},N}$, respectively.

As in [5], a set of parameters ν, G, and N will be said to be "in correspondence" if

$$\langle \mathcal{G}(\boldsymbol{u}) \rangle_\nu^{\mathcal{I},N} = G \tag{15}$$

G*a* is associated with a conserved, and therefore constant, quantity in the RNS model, while $\mathcal{G}$ is its irreversible counterpart in regular NS.

The adaptation of the two Gallavotti conjectures to our models can then be formulated as follows.

Conjecture 1. If ν, G, and N are in correspondence, then for any local observable (i.e., depending on a limited number of modes) $\mathcal{O}(\boldsymbol{u})$ one has

$$\forall N, \lim_{\nu \to 0} \langle \mathcal{O} \rangle_\mathcal{G}^{\mathcal{R},N} = \lim_{\nu \to 0} \langle \mathcal{O} \rangle_\nu^{\mathcal{I},N}. \tag{16}$$

Conjecture 2. Let $\mathcal{O}(\boldsymbol{u})$ be a local observable depending on $\boldsymbol{u}(\boldsymbol{k})$ for $k < K$, then if ν, G, and N are in correspondence one has

$$\lim_{N \to \infty} \langle \mathcal{O} \rangle_\mathcal{G}^{\mathcal{R},N} = \lim_{N \to \infty} \langle \mathcal{O} \rangle_\nu^{\mathcal{I},N}; \tag{17}$$

$\forall \nu$ and $K < c_\nu k_\eta$, $c_\nu \underset{\nu \to 0}{\longrightarrow} c_0 < \infty$, where k_η is the Kolmogorov scale.

Those two conjectures are associated with different regimes. Indeed, by fixing the resolution N and sending the viscosity to 0, one reaches the warm regime, characterized by thermalization (Conjecture 1). In contrast, by sending first the resolution N to infinity, then viscosity to 0, one prevents the thermalization from occurring (as it is associated with underresolved simulations). Therefore, Conjecture 2 is associated with hydrodynamical regimes and better describes turbulence in the limit of low viscosities.

2. Numerical procedure

In order to investigate the equivalence of ensemble, we start by running a LL-Navier-Stokes simulation, with time-independent viscosity of $\nu = 10^{-4}, 10^{-5}, 5\times10^{-6}, 10^{-6}, 10^{-7}$ for different values of N. After reaching a steady state for a sufficient number of time steps (to ensure the possibility of doing statistics), we use the LL-Navier-Stokes field as an initial condition for the LLRNS equation, in both conservation cases. We then let both reversible and irreversible simulations run for 4×10^5 time steps.

This procedure enables us to highlight any divergence of the reversible solution from the irreversible solution, while allowing us to characterize the simulations by viscosity ν or equivalently by their Reynolds number (Re).

3. Using scores to compare PDFs

In the next sections, we need to compare PDFs. To quantify their similarity, we introduce a scalar parameter, a score, defined as

$$\mathcal{S}(\mathcal{O}) = 1 - \sum_{i=1}^{p} \frac{|\mathcal{O}_\mathcal{R}^{(i)} - \mathcal{O}_\mathcal{I}^{(i)}|}{\mathcal{O}_\mathcal{I}^{(i)}} \mathcal{B}^{-i+1}, \tag{18}$$

where $\mathcal{O}^{(i)}$ stands for the ith moment of the local observable $\mathcal{O}$, p for the number of moments we take into account, and $\mathcal{B}$ for a decomposition basis ($\mathcal{B} = 10$, being a decimal basis in our case).

A score of one implies few errors between irreversible and reversible moments and leads to matching PDFs. We will restrict the computation of the score to the first three moments because of large statistical errors in our kurtosis. Therefore, the score should be roughly 1 whenever the three first moments coincide, i.e., whenever the distributions are identical around the mean value. Thus, $\mathcal{S}$ appears as a good indicator to qualify to what extent the conjecture holds.

4. Statistics of the reversible viscosity

Because of its presence in the limits, the viscosity plays a special role in the conjectures. However, it is a nonlocal observable. There is therefore no reason that mean reversible viscosities should be equivalent to irreversible viscosities,

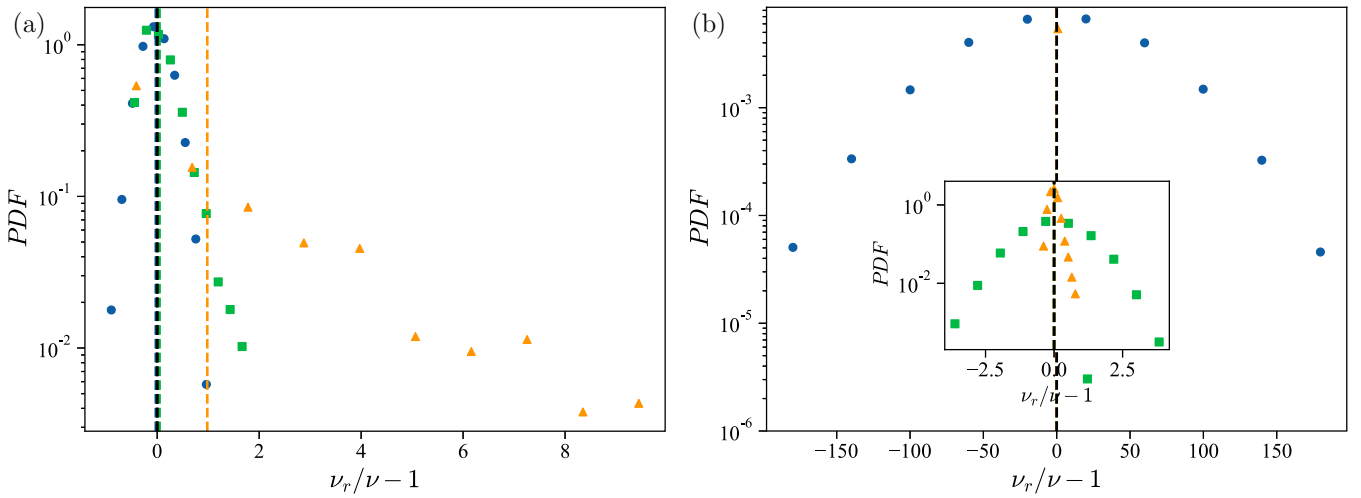

FIG. 8. PDF of the ratio $\nu_r/\nu - 1$ where ν_r stands for the reversible viscosity, for $N = 8^3$ (blue dots), 12^3 (green squares), 16^3 (orange diamonds), $\nu = 10^{-7}$. Panel (a) shows the results associated with $\mathcal{G} = E$, while panel (b) is associated with $\mathcal{G} = \Omega$. Colored dashed lines represent the mean values of the PDF, while the black dashed line is associated with $\langle \nu_r \rangle = \nu$.

even when only small values are considered. However, there are several differences between the conservation schemes that may temper this observation. First, the total kinetic energy is concentrated at the large scales, whereas enstrophy is a small-scale quantity, resulting in completely different statistics of the viscosity. In fact, a major difference between the two cases arises in the possible occurrence of negative viscosities. At low viscosities, there is almost no occurrence of negative viscosities in the conserved energy case, even in systems presenting a quasithermalized spectrum [Fig. 8(a)]. This is no longer true for the conserved enstrophy case as we observe many occurrences of negative viscosities in well-thermalized regimes [Fig. 8(b)].

In addition, conserving the enstrophy is a strong constraint, which implies additional equivalence for the viscosity. Indeed, if the first conjecture holds, we should observe conservation of the mean work of the forcing term $\mathcal{W} = \langle \boldsymbol{f}.\boldsymbol{u} \rangle$, because it is local at large scales (more details are in Sec. III H 1 and Tables V and VI in Appendix C). Using the energy budget, this yields $\langle \nu_r \rangle = \nu$ in the constant enstrophy case [5], even though ν_r is not a local observable. The property is not true for the conserved energy case, so that the Conjecture 1 should not hold *a priori* for the viscosity.

Our measurements are generally in agreement with these theoretical predictions, with some exceptions [Fig. 9(a)]. In the conserved enstrophy LLRNS model, we observe that the condition $\langle \nu_r \rangle = \nu$ holds for most values of ν, except for very low viscosity. In the conserved energy case, the situation is opposite: the property does not hold *a priori* for large enough values of viscosity. However, for small enough values of ν, we recover $\langle \nu_r \rangle \approx \nu$.

Note that since injection is a local observable, and since we are in a stationary state, where on average injection equals dissipation, we expect that $\nu_r \Omega$ obeys Conjectures 1 and 2. In the case of constant enstrophy, this condition is equivalent to $\langle \nu_r \rangle \approx \nu$, as we just saw. However, in the conserved energy case, this is not true anymore. Indeed, as we see in Fig. 9(b), we have $\langle \nu_r \Omega \rangle \approx \nu \langle \Omega \rangle$ for the conserved energy case, even though the equivalence is not fulfilled for the viscosity alone.

5. *Energy and enstrophy*

The first obvious quantities to investigate are energy E and enstrophy Ω. Results are reported in Tables V and VI (see Appendix C), where we give the mean ratios between reversible and irreversible values at various ν and for the two conservation schemes. In all cases, the ratio of $\langle \mathcal{G} \rangle / G$ is very close to 1, showing the validity of Eq. (15) for both conservation schemes. It is interesting to note that the mean energy is well described even in the conserved enstrophy case. On the other hand, in the conserved energy case the enstrophy is correctly reproduced only in the quasithermalized state [Table V and Fig. 6(a)]. In particular, at high resolution ($N = 16^3$), we observe an enstrophy ratio above 100%.

H. Analysis of Conjecture 1: Warm regime

In this subsection we focus on Conjecture 1. We consider various local quantities and analyze results at fixed number of modes $N = 8^3$ and decreasing viscosity of $\nu = 10^{-4}$, 10^{-5}, 5×10^{-6}, 10^{-6}, and 10^{-7}.

1. *Work of the forcing term*

We now consider the work $\mathcal{W} = \langle \boldsymbol{f} \cdot \boldsymbol{u} \rangle$. This quantity appears as a good candidate for Conjecture 1, as the forcing term is localized around $k_f = 15$ [see Eq. (14)]. Tables V and VI (see Appendix C) summarize the ratio of mean values between reversible and irreversible values, and show that almost all simulations fulfill correspondence conditions (15) with either conserved energy or conserved enstrophy. A finer understanding of this correspondence can be obtained by exploring the properties of its PDF in both the hydrodynamical case ($\nu = 10^{-4}$) and quasithermalized one ($\nu = 1\times10^{-6}$). This is shown in Fig. 10. In both cases and with both schemes, the PDF shows good agreement between the reversible and irreversible cases, except for the high-viscosity case, where tails are different. This difference is due to the difference in standard deviations. Nevertheless, in the quasithermalized regime [Fig. 10(b)], the PDF presents quasiperfect agreement

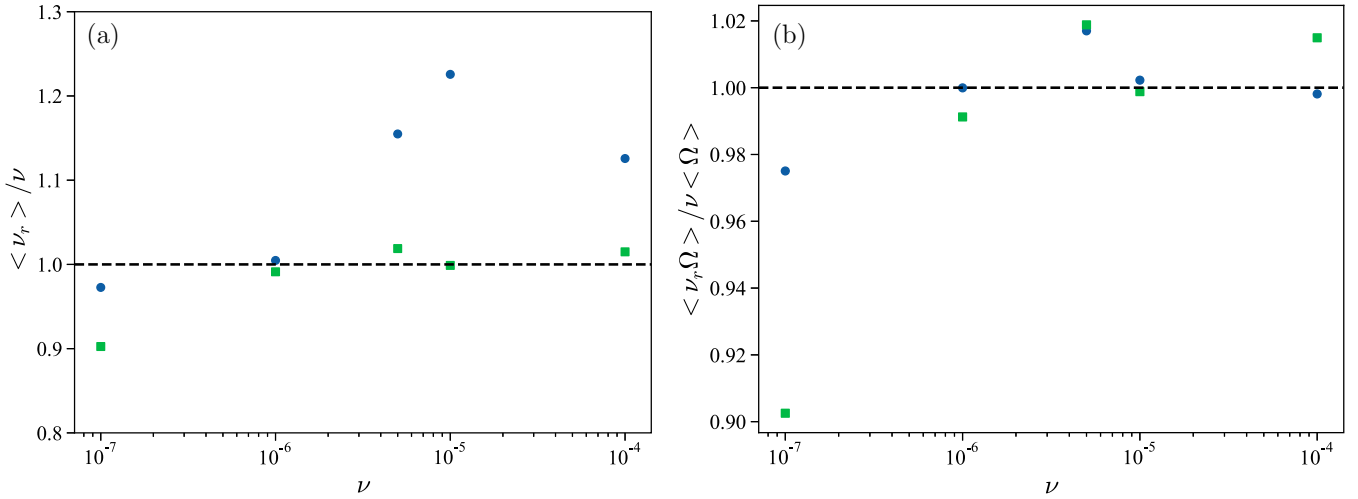

FIG. 9. Equivalence between the viscosities. (a) Ratio of the mean reversible viscosity over the standard NS viscosity. (b) Ratio of the mean dissipation $\nu\Omega$. Both figures are obtained for $N = 8^3$; blue dots correspond to conserved energy, while green squares are associated with conserved enstrophy.

between irreversible and reversible cases, which is a signature that Conjecture 1 holds for the local observable $\mathcal{W}$.

To further support this claim, we analyze the ratio of the two first-order moments $\frac{\langle \mathcal{W}_\mathcal{R} \rangle}{\langle \mathcal{W}_\mathcal{I} \rangle}$ and $\frac{\sigma^\mathcal{W}_\mathcal{R}}{\sigma^\mathcal{W}_\mathcal{I}}$. Figure 11 gathers those results, obtained for $N = 8^3$. One observes that for any value of ν, the mean value of $\mathcal{W}$ corresponds to the mean value of the reversible equations, within a 5% error margin [Fig. 11(a)]. This property does not hold, however, for the standard deviation, where the ratios lie outside the confidence interval in the hydrodynamical case [Fig. 11(b)]. As the viscosity decreases, both ratios enter the confidence interval, and thus both PDFs match in the inviscid limit.

2. *Energy spectra*

We now consider the equivalence for the distribution of energy in the wave number space, through the instantaneous energy spectra $E(\boldsymbol{k})$. As time varies, and for each given k, $E(k)$ fluctuates in time, and we can study its statistics through our score function. Figure 12 gathers the different scores $\mathcal{S}(E)$, obtained for different ν at various k_s. In the conserved energy case [Fig. 12(a)], Conjecture 1 holds quite well. Indeed, as $\nu \to 0$, the score is almost equal to one (purple pentagons) over the whole space, highlighting good moments matching. For higher viscosities (blue dots, green squares, etc.) the score starts to drop at smaller k, indicating that only the first shells display equivalence. Note that the statistics around the first and last data points might be biased by side effects associated with the sampling process. The conserved enstrophy case [Fig. 12(b)] shares some similar features, as the score indeed appears to grow as ν decreases, progressively spanning the whole grid.

According to the score, one should observe PDF matching (outside the tails) for $\nu = 10^{-4}$ at big scales ($k_s \approx 16.5$) and PDF differences at small scales ($k_s \approx 182.6$). This is indeed what we observe in Figs. 13(a) and 13(b). In addition, one expects nearly identical PDFs in both conservation schemes, at all scales for $\nu = 10^{-7}$. This statement is confirmed in

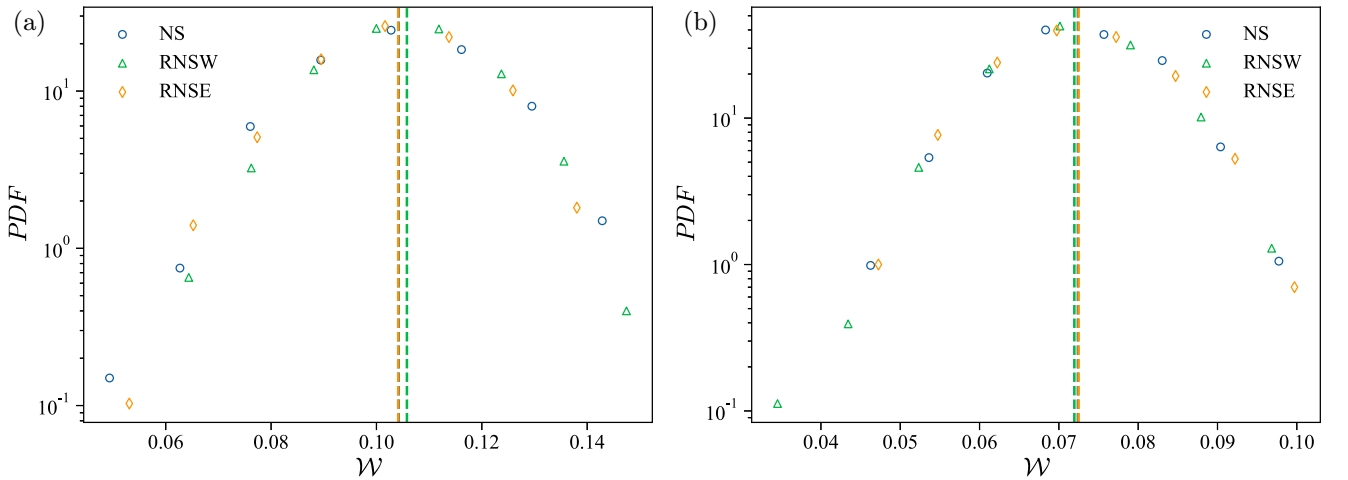

FIG. 10. PDF of the work of the forcing term $\mathcal{W}$. Simulations are performed with $N = 8^3$. (a) $\nu = 10^{-4}$, (b) $\nu = 10^{-6}$. Dashed lines represent the mean values of the PDF. Both conservation schemes show good agreement for the mean values. At higher viscosities, tails differ.

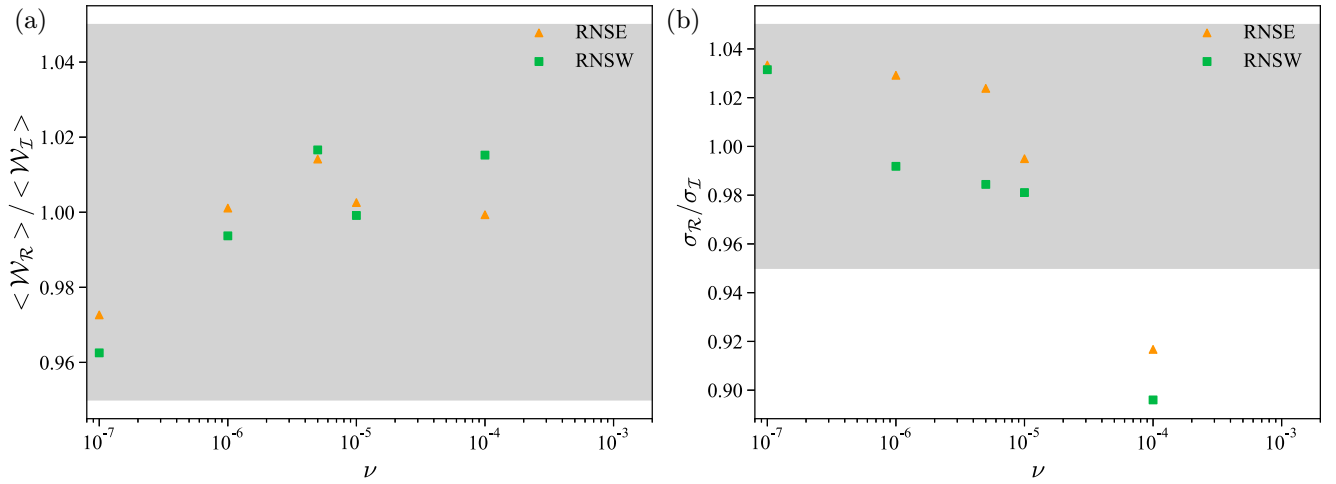

FIG. 11. Ratios of the two first moments of $\mathcal{W}$ as a function of the viscosity ν. Simulations are performed with $N = 8^3$. (a) Ratio $\langle\mathcal{W}_\mathcal{R}\rangle/\langle\mathcal{W}_\mathcal{I}\rangle$, (b) ratio $\sigma^\mathcal{W}_\mathcal{R}/\sigma^\mathcal{W}_\mathcal{I}$, where σ stands for the standard deviation. The gray shaded area represents the 5% confidence interval.

Figs. 13(c) and 13(d), where the PDFs are almost indistinguishable.

I. Analysis of Conjecture 2: Hydrodynamical regime

In this section we analyze Conjecture 2, i.e., equivalence at fixed ν and varying N in the case of the hydrodynamical regime, in the thermodynamic limit $h \to 0$ ($k_{\max} \to \infty$).

In the analysis of this conjecture, there appears a strong difference between the conserved energy case and the conserved enstrophy case. Indeed, the former case presents a phase transition whose characteristics depend on N (Fig. 6). This dependence complicates the analysis on the impact of $k_{\max} \to \infty$ ($N \to \infty$) in Conjecture 2. Indeed, for a given $\mathcal{R}_r$, increasing N implies a switching phase [Fig. 6(a)], going from quasithermalized regimes ($\mathcal{R}_r < \mathcal{R}^*_r$, in which Conjecture 1 holds) to hydrodynamical ones ($\mathcal{R}_r \geqslant \mathcal{R}^*_r$). Therefore, one must be careful while comparing similar Re for different resolutions as the validity of the conjecture is related to the position in the transition, as will be highlighted later.

1. Energy spectra

We now focus on the statistics of the energy spectrum at given values of k_s. In the hydrodynamical regime, Conjecture 2 implies that the score of $\mathcal{E}(k)$ should be equal to 1 in the thermodynamic limit $h \to 0$ ($k_{\max} \to \infty$). In practice, we shall see that this will be true only for a given range of wave number $k < K_\nu$ [5,24].

In the conserved enstrophy case the analysis is straightforward. We show in Fig. 14 the evolution of the score $\mathcal{S}_\Omega(E)$ at various resolutions. At lower resolution, $\mathcal{S}_\Omega(E)$ drops quickly (Fig. 14, blue dots) highlighting the absence of equivalence between the reversible and irreversible ensemble. By increasing N, we obtain scores closer to 1 on intervals up to K_ν, defined as the value of k such that $\forall k > K_\nu$, $\mathcal{S}_\mathcal{G}(\mathcal{O}) < 0.9$. We also observe that for low values of viscosity, the scores are

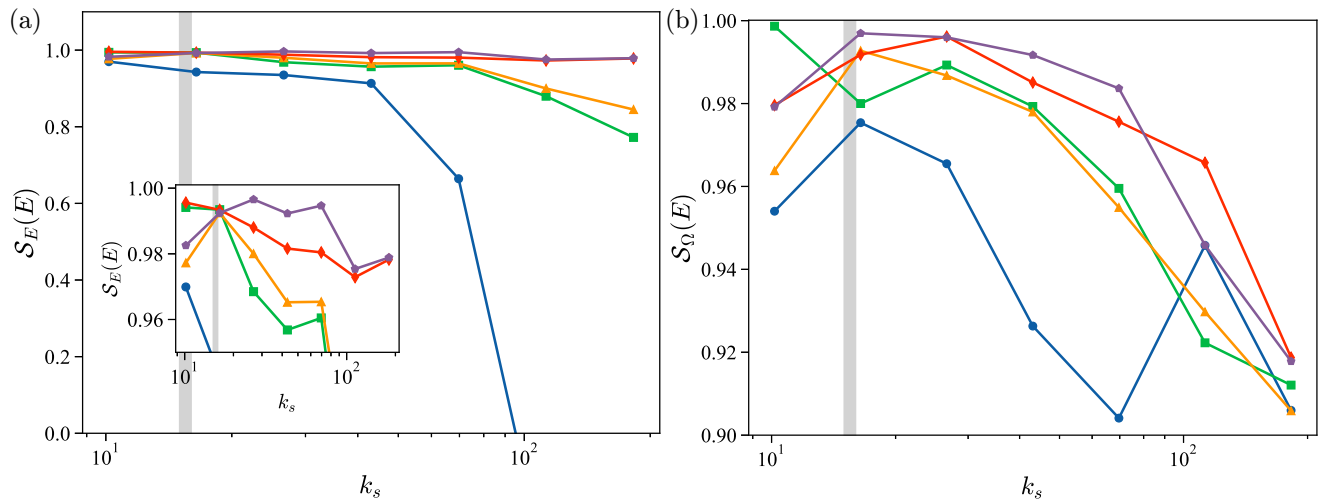

FIG. 12. Score $\mathcal{S}(E)$ of the energy in each shell. Panel (a) corresponds to the conserved energy case, while panel (b) is associated with the conserved enstrophy case. The gray shaded areas show where the forcing term is localized. Figures are obtained for $N = 8^3$. Blue dots, green squares, orange triangles, red diamonds, and purple pentagons are respectively associated with $\nu = 10^{-4}$, 10^{-5}, 5×10^{-6}, 10^{-6}, and 10^{-7}.

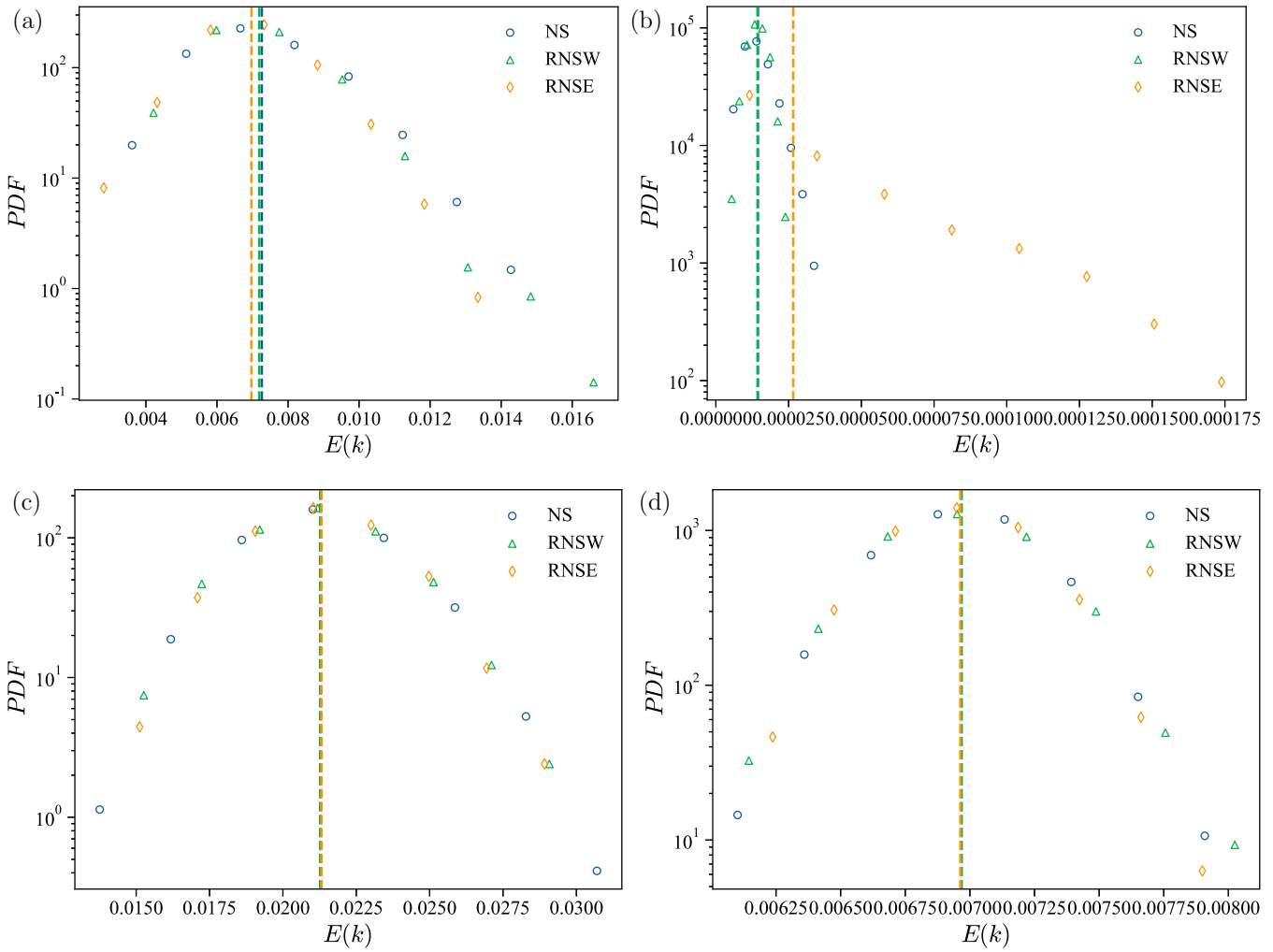

FIG. 13. Energy PDF. Results are obtained for different values of k_s and ν, with $N = 8^3$. (a), (b) $\nu = 10^{-4}$, $k_s \approx 16.5$, $k_s \approx 182.6$; (c), (d) $\nu = 10^{-7}$, $k_s \approx 16.5$, $k_s \approx 182.6$. Dashed lines represent the mean values of the PDF.

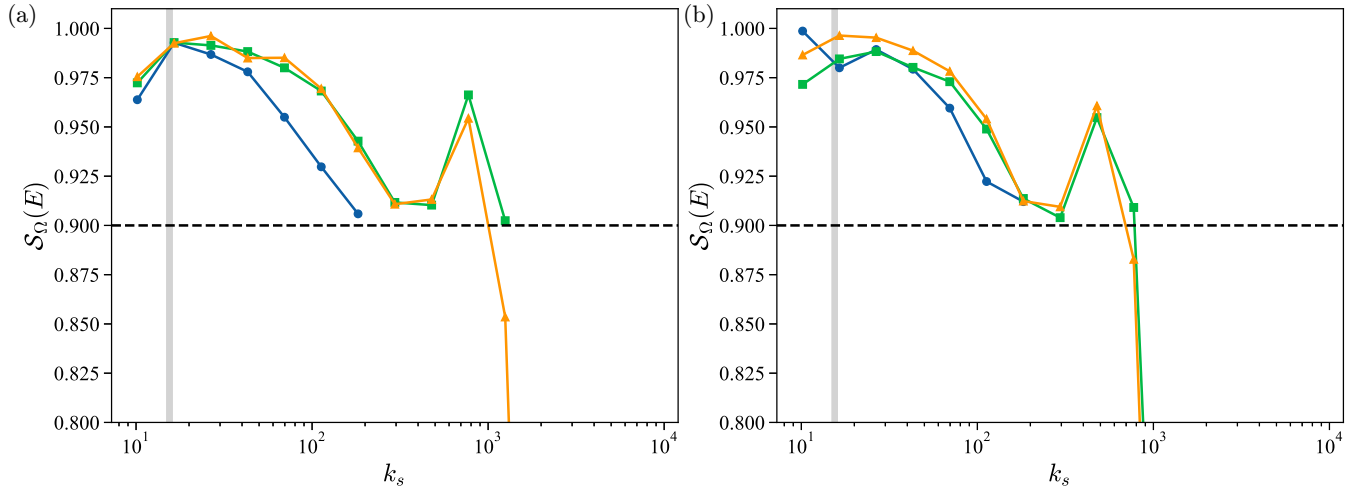

FIG. 14. Score $\mathcal{S}(E)$ of the energy in each shell for $\mathcal{G} = \Omega$. (a) $\nu = 5\times10^{-6}$; (b) $\nu = 10^{-5}$. Blue dots, green squares, and orange triangles correspond to $N = 8^3$, 12^3, 16^3, respectively. Black dashed lines correspond to a score of 0.9.

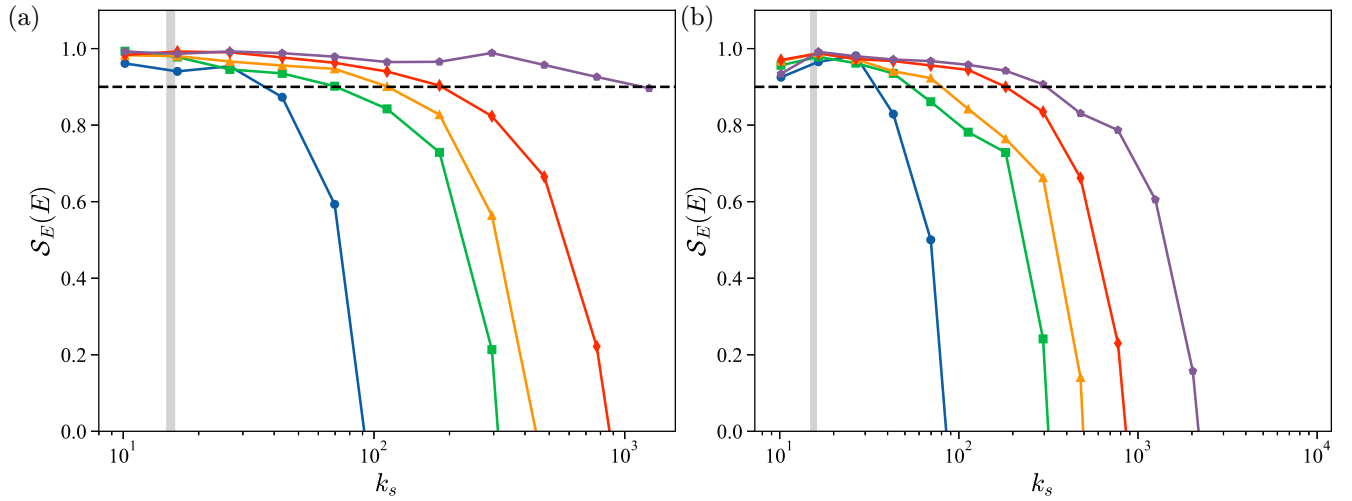

FIG. 15. Score $\mathcal{S}(E)$ of the energy in each shell for $\mathcal{G} = E$. (a) $N = 12^3$; (b) $N = 16^3$. Blue dots, green squares, orange triangles, red diamonds, and purple pentagons correspond to $\nu = 10^{-4}$, $\nu = 10^{-5}$, 5×10^{-6}, 10^{-6}, 10^{-7}, respectively. Note that in (a), the purple pentagons are associated with a quasithermalized state, being a crossover region between the two conjectures. Black dashed lines correspond to a score of 0.9.

similar for $N = 12^3$ and $N = 16^3$, supporting the second conjecture, in the conserved enstrophy case. For $k > K_\nu$, scores start to "oscillate," this is associated with the fact that the reversible moments fluctuate around the irreversible ones and sometimes lie in the confidence interval, leading to artificially higher scores.

In the conserved energy case, the analysis is complicated by the phase transition, as detailed below. According to Conjecture 2, one expects to observe scores $\mathcal{S}_\mathcal{G}(E) > 0.9$ on bigger and bigger domains as $\nu \to 0$. Figure 15 shows the scores, in the case of conserved energy E, for various viscosities and $N = 12^3$ [Fig. 15(a)] or $N = 16^3$ [Fig. 15(b)]. Our results indeed highlight a dependency of K_ν on ν (Figs. 14 and 15). Note that the red diamonds in Fig. 15(a) are associated with a crossover regime where thermalization at small scales starts to occur, leading to results similar to Conjecture 1 [Fig. 12(a)] but with a slight drop.

Figure 16 shows the extracted thresholds divided by the Kolmogorov scale for both conservation schemes, at different resolutions and different viscosities. Unlike in [5], c_ν is no longer a constant but depends on the value of ν and does not grow as fast as the Kolmogorov scale k_η (Fig. 16).

Note that for $\nu = 10^{-7}$, the $N = 12^3$ are underresolved, leading to an upper bound $K = k_{\max}$ for the threshold that cannot grow anymore as ν decreases. Such a phenomenon explains the difference between the two first points of Fig. 16(b).

In the thermodynamic limit of the conserved energy case, the equivalence is best achieved for $\mathcal{R}_r \to \mathcal{R}_r^*(N)$. As mentioned before, such properties make the comparison between resolutions difficult, as the value of $\mathcal{R}_r$ at which the transition

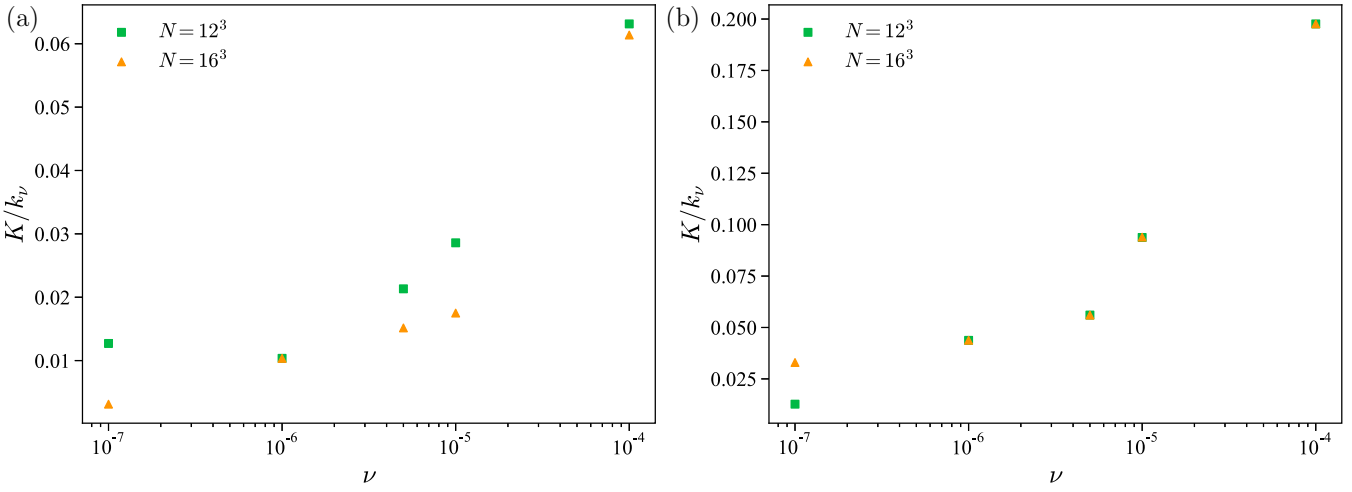

FIG. 16. Ratio K/k_ν in the context of Conjecture 2 (a) corresponds to conserved total kinetic energy, while (b) corresponds to conserved enstrophy. The thresholds K were extracted directly from the score at the considered k. The thresholds were not extracted for $N = 8^3$ since the resolution is insufficient as most simulations lie on the thermalized branch [Fig. 6(a), colored circles].

between warm and hydrodynamical regimes occurs also depends on N. Nevertheless, Fig. 16(a) gathers the results for the conserved energy case, confirming the validity of Conjecture 2, on smaller domains with respect to those observed in the conserved enstrophy case.

IV. CONCLUSION

We have shown that LLRNS models are able to reproduce features previously observed in DNS while allowing us to better probe the transition by reaching scales much lower than usual DNS. We found that the LLRNS system with conserved energy indeed exhibits a second-order phase transition, with $\sqrt{\Omega}$ as an order parameter, sharing interesting features with the reversible Leith model; a simple nonlinear diffusion model. The phase transition separates two phases, the first characterized by the coexistence between a hydrodynamical regime and an equipartition of energy at small scale (named the "warm" phase), and the second characterized by an overdamped regime with very large viscosity (named overdamped phase). In between, we have a turbulent hydrodynamical regime, with properties resembling those of solutions of the NS equations.

We have not observed a divergence of fluctuations in the LLRNS model with enstrophy conservation nor in models with fixed viscosity. This may be due to the fact that the enstrophy-conserving scheme is associated with more regular solutions than the energy-conserving scheme. In particular, it rules out a spontaneous reversal symmetry breaking mediated by dissipating singularities as conjectured by Onsager [1]. More work is therefore needed to understand the difference between the two conservation schemes from the point of view of the emergence of dissipative weak solutions. This is the subject of an ongoing work.

We also studied the finite-size corrections of the scalings induced by the finite resolution and found good agreement with tendencies predicted by the Leith model. Such a study would have been impossible to perform on present DNS. Finally, we studied the influence of reversibility on scalings of the ansatz of the structure functions. They were found to obey self-similar scaling in all phases, with an exponent ranging from 0.36 in the warm (reversible) phase to 0.42 in the hydrodynamical (irreversible) phase. We did not find any intermittency corrections in either phase. It is an open question whether choosing other step sizes on the logarithmic grid, for instance, allowing more interactions, will result in intermittency in either of the two phases.

We also tested the adaptation of two conjectures by Gallavotti [4], regarding the equivalence of the reversible models and the irreversible model. We find that the properties of the quasithermalized regime of the reversible and irreversible models are equivalent both for conserved enstrophy or conserved energy. This equivalence also holds in the hydrodynamical regime for local observables located at $k < K_\nu$, for both conserved enstrophy and conserved energy. This result is therefore an extension of the equivalence found in [5] in DNS of RNS with conserved enstrophy. In addition, we find that equivalence between irreversible LL-Navier-Stokes models and LLRNS models with conserved energy in fully developed turbulence (Conjecture 2) holds best in the limit $N \to \infty$, $\mathcal{R}_r \overset{>}{\to} \mathcal{R}_r^*$. This feature was discussed but not proven in [6] in the DNS case. We showed that, unlike in DNS [5], the value of $c_\nu = K/k_\nu$ is not a constant but depends on ν. Altogether, our results show that ensemble equivalence holds for LLRNS models in the average sense, since the conserved enstrophy and conserved energy model display similar means for all observables studied in this paper.

These results show the interest of the models based on projecting fluid dynamics on a log lattice. Being three-dimensional, and respecting most symmetries of the original equation, they may be used to explore fundamental issues of the original system, albeit at a moderate computational cost and without any adjustable parameters. By construction, they of course lack many interactions present in the original equations, and it is not clear how well many of the results presented here can be extended to real fluids. Nonetheless, it will likely take some time before direct numerical simulations can reach the parameter values explored here, so this interesting question is left for the future.

ACKNOWLEDGMENTS

This work received funding through the PhD fellowship programs of the Ecole Polytechnique and Ecole Normale Superieure Paris-Saclay, and through the ANR, via the grants ANR TILT Grant No. ANR-20-CE30-0035 and ANR BANG Grant No. ANR-22-CE30-0025.

APPENDIX A: VISCOUS SPLITTING

In our study we propose to first solve the inviscid NS equation (12), then we compute the reversible viscosity, according to the quantity that must be conserved. Finally, we take into account the viscosity by rescaling the velocity fields. One could wonder if this method gives proper results in the reversible case.

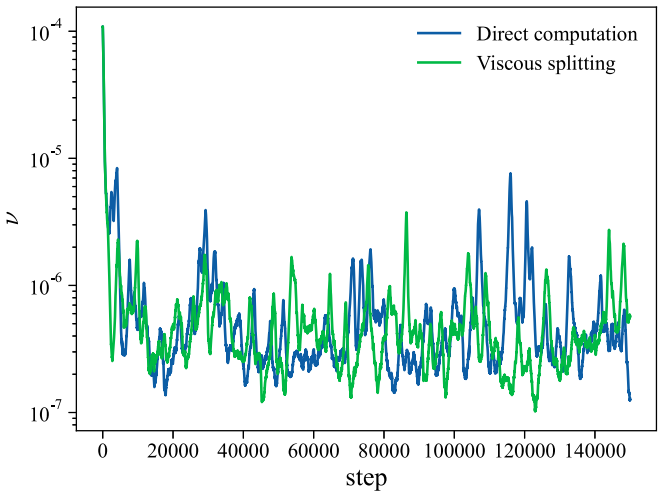

FIG. 17. Evolution of the reversible viscosity ν_r at each step. Both simulations are performed for $\lambda = \phi \approx 1.618$, $N = 12^3$, $f_0 = 0.27$. The green curve is obtained using the viscous splitting method, while the blue curve is obtained by directly solving the RNS equation, where the reversible viscosity is computed using Eq. (3).

TABLE V. Ratio of various quantities for constant energy. $\mathcal{W}$ stands for the work of the forcing term.

N	ν	$\langle E_\mathcal{R}\rangle/\langle E_\mathcal{I}\rangle$	$\langle \Omega_\mathcal{R}\rangle/\langle \Omega_\mathcal{I}\rangle$	$\langle W_\mathcal{R}\rangle/\langle W_\mathcal{I}\rangle$
	10^{-4}	100.0%	125.6%	99.9%
	10^{-5}	100.0%	102.1%	99.7%
8^3	5×10^{-6}	100.0%	98.2%	98.6%
	10^{-6}	100.0%	100.0%	99.9%
	10^{-7}	100.0%	100.0%	97.3%
	10^{-4}	100.0%	135.4%	99.6%
	10^{-5}	100.0%	160.0%	99.3%
12^3	5×10^{-6}	100.0%	164.6%	99.1%
	10^{-6}	100.0%	132.3%	99.7%
	10^{-7}	100.0%	100.4%	99.8%
	10^{-4}	100.0%	142.9%	97.5%
	10^{-5}	100.0%	156.1%	98.4%
16^3	5×10^{-6}	100.0%	145.1%	98.9%
	10^{-6}	100.0%	315.2%	98.8%
	10^{-7}	100.0%	313.4%	97.9%

TABLE VI. Ratio of various quantities for constant enstrophy. $\mathcal{W}$ stands for the work of the forcing term.

N	ν	$\langle E_\mathcal{R}\rangle/\langle E_\mathcal{I}\rangle$	$\langle \Omega_\mathcal{R}\rangle/\langle \Omega_\mathcal{I}\rangle$	$\langle W_\mathcal{R}\rangle/\langle W_\mathcal{I}\rangle$
	10^{-4}	98.2%	100.0%	98.5%
	10^{-5}	99.8%	100.0%	99.9%
8^3	5×10^{-6}	98.9%	100.0%	98.3%
	10^{-6}	99.8%	100.0%	99.4%
	10^{-7}	100.0%	100.0%	96.3%
	10^{-4}	98.5%	100.0%	98.1%
	10^{-5}	99.0%	100.0%	98.9%
12^3	5×10^{-6}	98.8%	100.0%	98.6%
	10^{-6}	98.6%	100.0%	98.9%
	10^{-7}	100.0%	100.0%	99.7%
	10^{-4}	98.8%	100.0%	98.0%
	10^{-5}	99.6%	100.0%	99.3%
16^3	5×10^{-6}	99.7%	100.0%	99.8%
	10^{-6}	99.5%	100.0%	99.8%
	10^{-7}	98.7%	100.0%	98.5%

Both methods lead to similar behavior of the viscosity (Fig. 17), with mean values $\nu_{r,\text{Splitting}} \approx 4.9\times10^{-7}$ and $\nu_{r,\text{Direct}} \approx 5.9\times10^{-7}$. It is expected to find a slight difference as the number of time step is still relatively small. Moreover, the direct computation is performed using the analytical expression of the reversible viscosity and therefore leads to deviation from E_0.

Still both methods give similar results (Fig. 17). However, the "viscous splitting" method allows us to "perfectly" (with floating-point accuracy) conserve a chosen quantity (here the total kinetic energy) without deviation.

APPENDIX B: ENSTROPHY RENORMALIZATION

The case of $\mathcal{R}_r \to 0$ is associated with a vanishing energy injection and therefore, in order to keep the total energy constant, to a vanishing viscosity. The system thus behaves as a truncated Euler equation and should exhibit an equipartition of energy. In our model this equipartition is characterized by an energy spectrum developing a power law k^{-1} that we will use in order to compute the total enstrophy $\Omega_{\max}$.

We start by assuming that the kinetic energy in a shell can be written as $E_k = \frac{A}{k}$, where A is a constant obtained through the total kinetic energy E_0:

$$E_0 = \sum_k E(k)\Delta\mu_k = A\sum_k \frac{1}{k}(\lambda k - k) = AN(\lambda - 1),$$

where $\Delta\mu_k$ is the measure of the space, which is $(\lambda k - k)$ for the 1D shells here. This leads to $A = \frac{E_0}{N(\lambda-1)}$, where N is the number of modes used on the grid.

We then compute the total enstrophy $\Omega_{\max}$:

$$\Omega_{\max} = \sum_k k^2 E(k)(\lambda k - k) = \frac{E_0}{N}\sum_k k^2$$

$$= \frac{E_0 k_0^2}{N}\sum_{p=0}^{N-1}\lambda^{2p} \simeq \frac{E_0\lambda^2 k_{\max}^2}{N(\lambda^2-1)}.$$

We can now define the renormalized enstrophy:

$$\widetilde{\Omega} = \frac{\Omega}{\Omega_{\max}}. \tag{B1}$$

APPENDIX C: TABLES

Containing the two tables, Tables V and VI.

[1] L. Onsager, Nuovo Cimento (1943–1954) **6**, 279 (1949).
[2] B. Dubrulle, J. Fluid Mech. **867**, P1 (2019).
[3] L. Kadanoff, D. Lohse, J. Wang, and R. Benzi, Phys. Fluids **7**, 617 (1995).
[4] G. Gallavotti, Phys. Lett. A **223**, 91 (1996).
[5] G. Margazoglou, L. Biferale, M. Cencini, G. Gallavotti, and V. Lucarini, Phys. Rev. E **105**, 065110 (2022).
[6] V. Shukla, B. Dubrulle, S. Nazarenko, G. Krstulovic, and S. Thalabard, Phys. Rev. E **100**, 043104 (2019).
[7] C. S. Campolina and A. A. Mailybaev, Nonlinearity **34**, 4684 (2021).
[8] C. Campolina, Master's thesis, Instituto de Matemática Pura e Aplicada (2019).
[9] P. Constantin, Bull. Am. Math. Soc. **44**, 603 (2007).
[10] C. Connaughton and S. Nazarenko, Phys. Rev. Lett. **92**, 044501 (2004).
[11] D. Bandak, N. Goldenfeld, A. A. Mailybaev, and G. Eyink, Phys. Rev. E **105**, 065113 (2022).
[12] L. Biferale, Annu. Rev. Fluid Mech. **35**, 441 (2003).
[13] T. Bohr, M. H. Jensen, G. Paladin, and A. Vulpiani, *Dynamical Systems Approach to Turbulence* (Cambridge University Press, Cambridge, 1998).

[14] M. H. Jensen, G. Paladin, and A. Vulpiani, Phys. Rev. A **43**, 798 (1991).
[15] M. De Pietro, L. Biferale, G. Boffetta, and M. Cencini, Eur. Phys. J. E **41**, 48 (2018).
[16] R. Benzi, S. Ciliberto, R. Tripiccione, C. Baudet, F. Massaioli, and S. Succi, Phys. Rev. E **48**, R29 (1993).
[17] S. Grossmann, D. Lohse, V. L'vov, and I. Procaccia, Phys. Rev. Lett. **73**, 432 (1994).
[18] U. Frisch, A. Pomyalov, I. Procaccia, and S. S. Ray, Phys. Rev. Lett. **108**, 074501 (2012).
[19] A. S. Lanotte, R. Benzi, S. K. Malapaka, F. Toschi, and L. Biferale, Phys. Rev. Lett. **115**, 264502 (2015).
[20] V. S. L'vov, E. Podivilov, A. Pomyalov, I. Procaccia, and D. Vandembroucq, Phys. Rev. E **58**, 1811 (1998).
[21] L. Biferale, A. Lambert, R. Lima, and G. Paladin, Physica D **80**, 105 (1995).
[22] C. S. Campolina and A. A. Mailybaev, Phys. Rev. Lett. **121**, 064501 (2018).
[23] Q. Pikeroen, A. Barral, G. Costa, C. Campolina, A. Mailybaev, and B. Dubrulle (unpublished).
[24] G. Gallavotti, Eur. Phys. J.: Spec. Top. **227**, 217 (2018).